

Planck intermediate results. XXVII. High-redshift infrared galaxy overdensity candidates and lensed sources discovered by Planck and confirmed by Herschel-SPIRE[★]

Planck Collaboration: N. Aghanim⁵⁴, B. Altieri³⁵, M. Arnaud⁶⁶, M. Ashdown^{63,6}, J. Aumont⁵⁴, C. Baccigalupi⁷⁹, A. J. Banday^{88,10}, R. B. Barreiro⁵⁹, N. Bartolo^{27,60}, E. Battaner^{90,91}, A. Beelen⁵⁴, K. Benabed^{55,87}, A. Benoit-Lévy^{21,55,87}, J.-P. Bernard^{88,10}, M. Bersanelli^{30,47}, M. Bethermin⁶⁶, P. Bielewicz^{88,10,79}, L. Bonavera⁵⁹, J. R. Bond⁹, J. Borrill^{13,83}, F. R. Bouchet^{55,81}, F. Boulanger^{54,78}, C. Burigana^{46,28,48}, E. Calabrese⁸⁶, R. Canameras⁵⁴, J.-F. Cardoso^{67,1,55}, A. Catalano^{68,65}, A. Chamballu^{66,14,54}, R.-R. Chary⁵², H. C. Chiang^{24,7}, P. R. Christensen^{75,33}, D. L. Clements⁵¹, S. Colombi^{55,87}, F. Couchot⁶⁴, B. P. Crill^{61,76}, A. Curto^{6,59}, L. Danese⁷⁹, K. Dassas⁵⁴, R. D. Davies⁶², R. J. Davis⁶², P. de Bernardis²⁹, A. de Rosa⁴⁶, G. de Zotti^{43,79}, J. Delabrouille¹, J. M. Diego⁵⁹, H. Dole^{54,53}, S. Donzelli⁴⁷, O. Dore^{61,11}, M. Douspis⁵⁴, A. Ducout^{55,51}, X. Dupac³⁶, G. Efstathiou⁵⁷, F. Elsner^{21,55,87}, T. A. Enßlin⁷², E. Falgarone⁶⁵, I. Flores-Cacho^{10,88}, O. Forni^{88,10}, M. Frailis⁴⁵, A. A. Fraisse²⁴, E. Franceschi⁴⁶, A. Frejsel⁷⁵, B. Frye⁸⁵, S. Galeotta⁴⁵, S. Galli⁵⁵, K. Ganga¹, M. Giard^{88,10}, E. Gjerløw⁵⁸, J. González-Nuevo^{59,79}, K. M. Górski^{61,92}, A. Gregorio^{31,45,50}, A. Gruppuso⁴⁶, D. Guéry⁵⁴, F. K. Hansen⁵⁸, D. Hanson^{73,61,9}, D. L. Harrison^{57,63}, G. Helou¹¹, C. Hernández-Monteagudo^{12,72}, S. R. Hildebrandt^{61,11}, E. Hivon^{55,87}, M. Hobson⁶, W. A. Holmes⁶¹, W. Hovest⁷², K. M. Huffenberger²², G. Hurier⁵⁴, A. H. Jaffe⁵¹, T. R. Jaffe^{88,10}, E. Keihänen²³, R. Keskitalo¹³, T. S. Kisner⁷⁰, R. Kneissl^{34,8}, J. Knoch⁷², M. Kunz^{16,54,2}, H. Kurki-Suonio^{23,41}, G. Lagache^{5,54}, J.-M. Lamarre⁶⁵, A. Lasenby^{6,63}, M. Lattanzi²⁸, C. R. Lawrence⁶¹, E. Le Floch⁶⁶, R. Leonardi³⁶, F. Levrier⁶⁵, M. Liguori^{27,60}, P. B. Lilje⁵⁸, M. Linden-Vørnle¹⁵, M. López-Caniego^{36,59}, P. M. Lubin²⁵, J. F. Macías-Pérez⁶⁸, T. MacKenzie²⁰, B. Maffei⁶², N. Mandolesi^{46,4,28}, M. Maris⁴⁵, P. G. Martin⁹, C. Martinache⁵⁴, E. Martínez-González⁵⁹, S. Masi²⁹, S. Matarrese^{27,60,39}, P. Mazzotta³², A. Melchiorri^{29,49}, A. Mennella^{30,47}, M. Migliaccio^{57,63}, A. Moneti⁵⁵, L. Montier^{88,10}, G. Morgante⁴⁶, D. Mortlock⁵¹, D. Munshi⁸⁰, J. A. Murphy⁷⁴, P. Natoli^{28,3,46}, M. Negrello⁴³, N. P. H. Nesvadba⁵⁴, D. Novikov⁷¹, I. Novikov^{75,71}, A. Omont⁵⁵, L. Pagano^{29,49}, F. Pajot⁵⁴, F. Pasian⁴⁵, O. Perdereau⁶⁴, L. Perotto⁶⁸, F. Perrotta⁷⁹, V. Pettorino⁴⁰, F. Piacentini²⁹, M. Piat¹, S. Ptaszyński⁶⁴, E. Pointecouteau^{88,10}, G. Polenta^{3,44}, L. Popa⁵⁶, G. W. Pratt⁶⁶, S. Prunet^{55,87}, J.-L. Puget⁵⁴, J. P. Rachen^{19,72}, W. T. Reach⁸⁹, M. Reinecke⁷², M. Remazeilles^{62,54,1}, C. Renault⁶⁸, I. Ristorcelli^{88,10}, G. Rocha^{61,11}, G. Roudier^{1,65,61}, B. Rusholme⁵², M. Sandri⁴⁶, D. Santos⁶⁸, G. Savini⁷⁷, D. Scott²⁰, L. D. Spencer⁸⁰, V. Stolyarov^{6,63,84}, R. Sunyaev^{72,82}, D. Sutton^{57,63}, J.-F. Sygnet⁵⁵, J. A. Tauber³⁷, L. Terenzi^{38,46}, L. Toffolatti^{17,59,46}, M. Tomasi^{30,47}, M. Tristram⁶⁴, M. Tucci¹⁶, G. Umata⁴², L. Valenziano⁴⁶, J. Valiviita^{23,41}, I. Valtchanov³⁵, B. Van Tent⁶⁹, J. D. Vieira^{11,18}, P. Vielva⁵⁹, L. A. Wade⁶¹, B. D. Wandelt^{55,87,26}, I. K. Wehus⁶¹, N. Welikala⁸⁶, A. Zacchei⁴⁵, and A. Zonca²⁵

(Affiliations can be found after the references)

Submitted 11 Aug 2014 / Accepted 13 March 2015

Abstract

We have used the *Planck* all-sky submillimetre and millimetre maps to search for rare sources distinguished by extreme brightness, a few hundred millijanskies, and their potential for being situated at high redshift. These “cold” *Planck* sources, selected using the High Frequency Instrument (HFI) directly from the maps and from the Planck Catalogue of Compact Sources (PCCS), all satisfy the criterion of having their rest-frame far-infrared peak redshifted to the frequency range 353 – 857 GHz. This colour-selection favours galaxies in the redshift range $z = 2-4$, which we consider as cold peaks in the cosmic infrared background. With a 4.5 beam at the four highest frequencies, our sample is expected to include overdensities of galaxies in groups or clusters, lensed galaxies, and chance line-of-sight projections. We perform a dedicated *Herschel*-SPIRE follow-up of 234 such *Planck* targets, finding a significant excess of red 350 and 500 μm sources, in comparison to reference SPIRE fields. About 94 % of the SPIRE sources in the *Planck* fields are consistent with being overdensities of galaxies peaking at 350 μm , with 3 % peaking at 500 μm , and none peaking at 250 μm . About 3 % are candidate lensed systems, all 12 of which have secure spectroscopic confirmations, placing them at redshifts $z > 2.2$. Only four targets are Galactic cirrus, yielding a success rate in our search strategy for identifying extragalactic sources within the *Planck* beam of better than 98 %. The galaxy overdensities are detected with high significance, half of the sample showing statistical significance above 10σ . The SPIRE photometric redshifts of galaxies in overdensities suggest a peak at $z \approx 2$, assuming a single common dust temperature for the sources of $T_d = 35$ K. Under this assumption, we derive an infrared (IR) luminosity for each SPIRE source of about $4 \times 10^{12} L_\odot$, yielding star formation rates of typically $700 M_\odot \text{yr}^{-1}$. If the observed overdensities are actual gravitationally-bound structures, the total IR luminosity of all their SPIRE-detected sources peaks at $4 \times 10^{13} L_\odot$, leading to total star formation rates of perhaps $7 \times 10^3 M_\odot \text{yr}^{-1}$ per overdensity. Taken together, these sources show the signatures of high- z ($z > 2$) protoclusters of intensively star-forming galaxies. All these observations confirm the uniqueness of our sample compared to reference samples and demonstrate the ability of the all-sky *Planck*-HFI cold sources to select populations of cosmological and astrophysical interest for structure formation studies.

Key words. Galaxies: high-redshift, clusters, evolution, star formation – Cosmology: observations, large-scale structure of Universe – Submillimetre: galaxies – Gravitational lensing: strong

1. Introduction

Cosmological structure formation in the linear regime is now fairly well constrained by observations at the largest scales (e.g.,

[★] corresponding author e-mail: herve.dole@ias.u-psud.fr

Tegmark et al. 2004, Cole et al. 2005). In the non-linear regime the situation is less clear because structure formation becomes a complex interplay between dark matter collapse and the hydrodynamics of baryonic cooling. In the particularly dense environs of the most massive dark matter halos, this interplay should lead to vigorous episodes of rapid star formation and galaxy growth, giving rise to copious amounts of FIR (far-infrared) emission from dust heated by young stellar populations in massive galaxies during periods of intense star formation.

From the standpoint of galaxy evolution, studying this intense star formation epoch in massive dark matter halos may provide a wealth of observational constraints on the kinematics and evolutionary history of galaxies in massive galaxy clusters, as well as the intracluster gas. From the point of view of cosmology, clusters yield information on non-Gaussianities of primordial fluctuations and can challenge the Λ CDM (cold dark matter) model (Brodwin et al. 2010; Hutsi 2010; Williamson et al. 2011; Harrison & Coles 2012; Holz & Perlmutter 2012; Waizmann et al. 2012; Trindade et al. 2013), while lensed sources act as probes of dark matter halos, and both are probes of cosmological parameters such as Ω_M (matter density today divided by the critical density of the Universe) and σ_8 (the rms fluctuation in total matter – baryons + CDM + massive neutrinos – in $8 h^{-1}$ Mpc spheres today at $z = 0$) (Planck Collaboration XVI 2014). Furthermore, clusters of galaxies are crucial objects that bridge astrophysics and cosmology, sometimes with some tensions, particularly regarding the measurement of σ_8 (Planck Collaboration XVI 2014; Planck Collaboration XX 2014; Planck Collaboration I 2015; Planck Collaboration XIII 2015), all of which has led to a debate between cluster phenomenology and cosmological physics.

The extragalactic sky in the submillimetre (submm) and millimetre (mm) regime has been of considerable scientific interest for over two decades, with the distinct advantage that the steep rise in the redshifted Rayleigh-Jeans tail of the modified blackbody emitted by the warm dust in infrared galaxies largely compensates for cosmological dimming, the “negative k-correction” (Franceschini et al. 1991; Blain & Longair 1993; Guiderdoni et al. 1997). As a consequence, the flux density of galaxies depends only weakly on redshift, opening up a particularly interesting window into the high-redshift Universe (typically $2 < z < 6$). Constant improvements in bolometer technology have led to impressive samples of high- z galaxies being identified with ground-based, balloon and space-borne telescopes (e.g., Hughes et al. 1998; Barger et al. 1998; Chapman et al. 2005; Lagache et al. 2005; Patanchon et al. 2009; Devlin et al. 2009; Chapin et al. 2009; Negrello et al. 2010; Vieira et al. 2010; Oliver et al. 2010; Eales et al. 2010).

Nevertheless, only with the recent advent of wide-field surveys with astrophysical and cosmological scope have the systematic searches become efficient enough to identify the brightest of these objects with flux densities above about 100 mJy at $350 \mu\text{m}$, e.g., with *Herschel*¹ (Pilbratt et al. 2010; Eales et al. 2010; Oliver et al. 2010), the South Pole Telescope (Vieira et al. 2010), *WISE* (Wright et al. 2010; Stanford et al. 2014), and *Spitzer* (Papovich 2008; Stanford et al. 2012). Such sources are very rare. For example, the surface density of red sources brighter than 300 mJy at $500 \mu\text{m}$ is 10^{-2} deg^{-2} for strongly lensed galaxies, $3 \times 10^{-2} \text{ deg}^{-2}$ for AGN (active galactic nuclei, here radio-loud, mostly blazars), and 10^{-1} deg^{-2} for late-

type galaxies at moderate redshifts (e.g., Negrello et al. 2007, 2010). Other models predict similar trends (Paciga et al. 2009; Lima et al. 2010; Bethermin et al. 2011; Hezaveh et al. 2012). This makes even relatively shallow submm surveys interesting for searches of high-redshift objects, as long as they cover large parts of the sky. Studies of gravitationally lensed galaxies at high redshifts originating from these surveys (Negrello et al. 2010; Combes et al. 2012; Busmann et al. 2013; Herranz et al. 2013; Rawle et al. 2014; Wardlow et al. 2013) illustrate the scientific potential of such surveys for identifying particularly interesting targets for a subsequent detailed characterization of high- z star formation through multi-wavelength follow-up observations.

The power of wide-field surveys in detecting the rarest objects on the submm sky is even surpassed with genuine all-sky surveys, which systematically and exhaustively probe the brightest objects in their wavelength domain down to their completeness limits. Here we present a search for the rarest, most extreme high-redshift ($z \gtrsim 2$) candidates on the submillimetre sky, which was performed with the *Planck*² all-sky survey (Planck Collaboration I 2014, 2015). The *Planck* Catalogue of Compact Sources (PCCS, Planck Collaboration XXVIII 2014) has a completeness limit of about 600 mJy at the highest frequencies, which corresponds to $L_{\text{FIR}} \simeq 5 \times 10^{13} L_{\odot}$ at $z = 2$. With a $5'$ beam (Planck Collaboration VII 2014) at the four highest frequencies (corresponding to a physical distance of about 2.5 Mpc at $z = 2$), we expect that sources with bona fide colours of high- z galaxies in the *Planck*-HFI bands are either strongly gravitationally lensed galaxies, or the combined dust emission of multiple galaxies in a shared vigorously star-forming environment in the high redshift Universe. The latter case is consistent with the result that submm galaxies or ULIRGs (Ultra Luminous Infrared Galaxies) are strongly clustered (Blain et al. 2004; Farrah et al. 2006; Magliocchetti et al. 2007; Austermann et al. 2009; Santos et al. 2011; Ivison et al. 2012; Valtchanov et al. 2013; Noble et al. 2013; Clements et al. 2014), and may include massive galaxy clusters during their major growth phase. It is also possible of course that the sources are chance alignments of multiple high-redshift galaxies projected onto the same line of sight (Negrello et al. 2005, 2007, 2010; Chiang et al. 2013), or of multiple, lower-mass galaxy groups or clusters.

Identifying high-redshift cluster candidates directly by the signatures of their total star formation is a very useful complement to the diagnostics used to identify galaxy clusters so far. Most systematic searches today focus on the primary constituents of more evolved, lower-redshift clusters, like their populations of massive, passively evolving galaxies (‘red-sequence galaxies’), the hot intracluster medium (either through X-ray emission or the Sunyaev-Zeldovich effect), or the suspected progenitors of today’s brightest cluster galaxies, in particular high-redshift galaxies (Steidel et al. 2000; Brand et al. 2003; Kodama et al. 2007; Scoville et al. 2007; Venemans et al. 2007; Papovich 2008; Daddi et al. 2009; Brodwin et al. 2010; Galametz et al. 2010; Papovich et al. 2010; Capak et al. 2011; Hatch et al. 2011; Kuiper et al. 2011; Ivison et al. 2013; Muzzin et al. 2013; Wylezalek et al. 2013a; Chiang et al. 2014; Cooke et al. 2014; Cucciati et al. 2014; Mei et al. 2014; Rettura et al. 2014, for instance). With the limited sensitivity and the large beam of

² *Planck* is a project of the European Space Agency – ESA – with instruments provided by two scientific Consortia funded by ESA member states (in particular the lead countries: France and Italy) with contributions from NASA (USA), and telescope reflectors provided in a collaboration between ESA and a scientific Consortium led and funded by Denmark.

¹ *Herschel* is an ESA space observatory with science instruments provided by European-led Principal Investigator consortia and with important participation from NASA.

PLCK G256.8-33.2

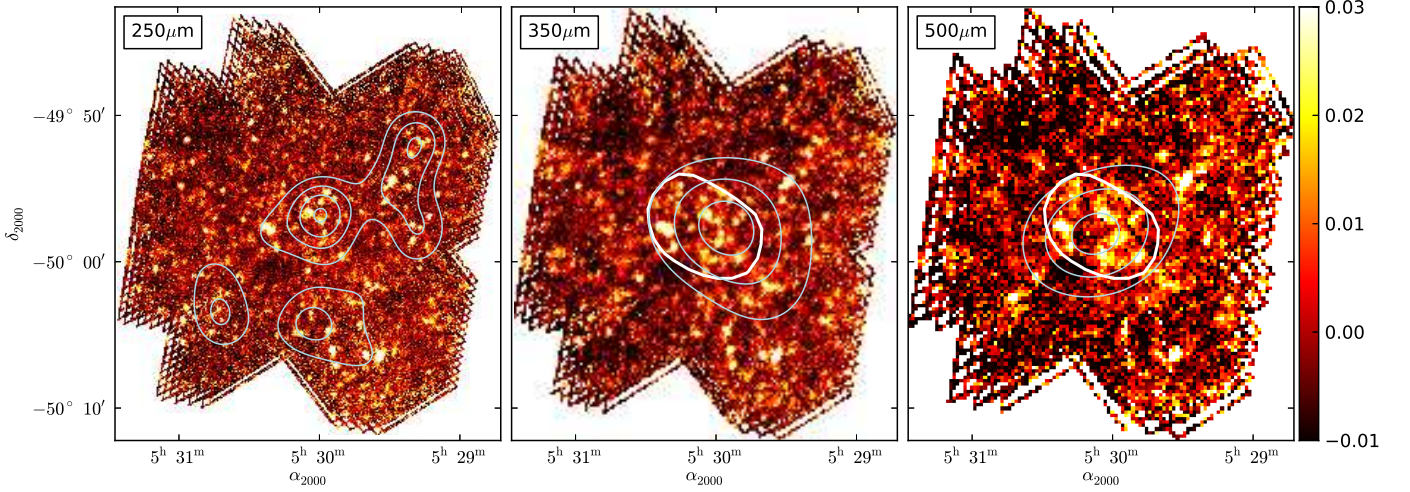


Figure 1. SPIRE maps at 250, 350, and 500 μm of one typical overdensity in our sample (a *Planck* cold source of the CIB – Cosmic Infrared Background). The thick white contour at 350 μm shows the *Planck* IN region at 857 GHz, and the same is true for the map at 500 μm at 545 GHz (i.e., the 50 % contour of the *Planck* source maximum). Thin contours correspond to the overdensity of SPIRE sources at each wavelength, marked at 2σ , 3σ , etc. (see Sect. 4.2 for details). SPIRE identifies a few (typically 5 to 10) sources inside the *Planck* contour. We use these contours to separate the IN and OUT zones. These data come from a $7' \times 7'$ SPIRE scan (see Table 1 and Sect. 2.3).

PLCK G244.8+54.9

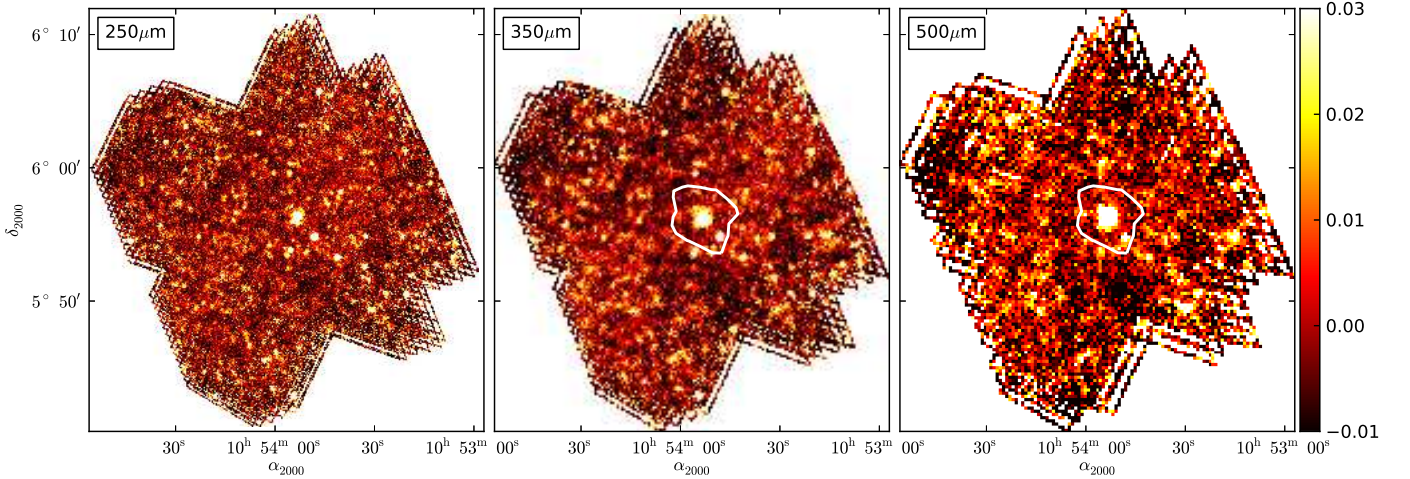


Figure 2. SPIRE maps at 250, 350, and 500 μm for a lensed source. In this case a single very bright SPIRE source is detected. This source is confirmed at the Jy level and has a redshift of $z = 3.0$, measured from multi-line spectroscopy acquired at IRAM using EMIR (Canameras 2015). The white contour is the *Planck* IN region, defined in the same way as in Fig. 1. These data come from a $7' \times 7'$ SPIRE scan (see Table 1 and Sect. 2.3).

Planck, in turn, we effectively select the most intensely star-forming Mpc-scale environments in the high-redshift Universe.

Using *Planck*, we have selected putative high-redshift objects with spectral energy distributions (SEDs) of warm dust, peaking between observed frequencies of 353 and 857 GHz. This has a net effect of selecting sources either peaking at 545 GHz, or to a lesser extent sources having their infrared peak between 353 and 857 GHz. This equates, in principle, to redshifted infrared galaxies at $z \sim 2-4$. We refer to these as “cold” sources of the Cosmic Infrared Background (or CIB), which have a red and thus potentially redshifted SED. The CIB (Puget et al. 1996; Hauser et al. 1998; Hauser & Dwek 2001; Dole et al. 2006; Planck Collaboration XXX 2014) is the in-

tegrated relic emission in the broad infrared range, typically $8\mu\text{m}$ to 1 mm, where the emission reaches a maximum (Dole et al. 2006). Physically, such objects correspond to galaxy and AGN formation and evolutionary processes, and more generally the history of energy production in the post-recombination Universe (e.g., Kashlinsky 2005; Planck Collaboration XVIII 2011). The CIB, as observed in the submillimetre, is considered as a proxy for intense star formation at redshifts $z > 1$ (Planck Collaboration XXX 2014) as well as for the mass of structures (Planck Collaboration XVIII 2014).

The *Planck* collaboration has also released the PCCS (Planck Collaboration XXVIII 2014), containing 24381 sources at 857 GHz, with 7531 sources at Galactic latitudes $|b| > 30^\circ$, of

which many are of interest for extragalactic studies. The main difference between the cold sources of the CIB and the red sources of the PCCS (both used in this work) can be summarized as a threshold difference: cold CIB sources are detected in the CIB fluctuations with a combined spectral and angular filtering method (Montier et al. 2010), while PCCS sources are detected independently in the frequency maps using an angular filtering method with a higher threshold (Planck Collaboration XXVIII 2014).

This paper presents the observations and analysis of our extensive dedicated *Herschel*-SPIRE (Griffin et al. 2010) follow-up of 234 *Planck* sources (either selected from the CIB fluctuations or from the PCCS). The paper is structured into seven sections. In Sect. 2, we detail the *Planck* parent sample and the *Herschel* observations. Section 3 gives a technical description of the algorithms used in the generation of the SPIRE photometry and the catalogue. In Sect. 4 we use statistics to characterize the *Herschel* observations; in particular we quantify the overdensities and the colours of the SPIRE counterparts and propose a classification of either overdensities or lensed candidates. In Sect. 5, we discuss the properties of the lensed source candidates, while in Sect. 6 we focus on the overdensities and their characterization, including a stacking analysis. Conclusions are reported in Sect. 7. The Appendices contain information on the SPIRE catalogue generation and the number counts, and a gallery of sample fields. We use the *Planck* 2013 cosmology (Planck Collaboration XVI 2014, table 5: *Planck*+WP+highL+BAO) throughout the paper.

2. Sample selection and observations

2.1. *Planck* observations and selection

*Planck*³ observed the whole sky at frequencies between 30 and 857 GHz (Planck Collaboration I 2014). We made two different selections to follow-up with *Herschel*: first, using the maps and looking for cold sources of the CIB; second, using the public catalogue of compact sources (PCCS).

2.1.1. Cold sources of the CIB in the *Planck* maps

We make use of the *Planck*-HFI (High Frequency Instrument, Planck Collaboration VI 2014) data as well as the *IRAS*/*IRIS* data (Miville-Deschênes & Lagache 2005) at 100 μm . For this purpose we use the cleanest 26% of the sky (in the *Planck* 857 GHz map), defined by a minimal cirrus contamination, $N_{\text{HI}} < 3 \times 10^{20} \text{cm}^{-2}$. The detection and selection algorithm, based on Montier et al. (2010) can be summarized in the following seven steps (Planck Collaboration 2015).

- (i) *CMB cleaning*: the 143 GHz *Planck*-HFI map is extrapolated to the other bands according to a CMB spectrum and removed from the maps at other frequencies.
- (ii) *Galactic cirrus cleaning*: the *IRAS*/*IRIS* 100 μm map, considered as a “warm template” of Galactic cirrus, is extrapolated to the *Planck*-HFI bands, taking into account the local colour, and removed from the maps following the prescription of the CoCoCoDeT algorithm (Montier et al. 2010).
- (iii) *Construction of excess maps*: the 545 GHz excess map is defined as the difference between the cleaned 545 GHz

³ *Planck* data (maps and catalogues) can be downloaded from the *Planck* Legacy Archive <http://pla.esac.esa.int/pla/aio/planckProducts.html>

Table 1. SPIRE programmes following-up *Planck* cold sources of the CIB. HPASSS is composed of 124 sources selected from the maps (two were repeated, so 126 fields), together with 28 from the PCCS (four were cirrus dominated, so 24 net fields). A total of 228 sources are useable (Sect. 2.2).

Programme	No. of fields	Map size	AOR ^a time
OT1	10	15' \times 15'	3147 s
OT2	70	7' \times 7'	838 s
HPASSS . . .	124 (126) (9 ^b) + 24 (28)	7' \times 7'	838 s
Total	228 (234)		

^a Astronomical Observation Request.

^b Nine HPASSS sources are from archival data.

- map and a power law interpolated between the cleaned maps at 857 GHz and 353 GHz.
- (iv) *Point source detection in the excess maps*: we apply a Mexican hat type detection algorithm (González-Nuevo et al. 2006) with a size parameter of $R = 5'$ in the 545 GHz excess maps.
- (v) *Single frequency detection*: we also require a detection in each cleaned map at 857 and 353 GHz.
- (vi) *Colour-colour selection*: we apply two criteria on the S_{545}/S_{857} (i.e., 545 GHz to 857 GHz) and S_{353}/S_{545} (i.e., 353 GHz to 545 GHz) flux density ratios to select the reddest sources.

This produces a dozen hundred candidates on the cleanest 26% region of the submm sky. We note that this procedure has been set-up early on in the *Planck* project. The final catalog of *Planck* high- z candidates is being generated using a similar (but not exactly identical) method which will be described in a forthcoming paper (Planck Collaboration 2015). In particular, the CMB estimate will not be the 143 GHz HFI map, but instead the CMB derived by component separation. The present paper focuses on the first candidates followed up by *Herschel*.

2.1.2. *Planck* PCCS sources

We make use of the PCCS to choose a sample of high- z sources selected by the expected peak in their thermal dust spectrum in the rest-frame far infrared. Our four step procedure here is based on the work of Negrello et al. (2010). First of all, we use the 857 GHz Galactic mask, keeping 52% of the sky (Planck Collaboration Int. VII 2013). Secondly, we select all the sources with $S/N > 4$ at 545 GHz and the colours $S_{857}/S_{545} < 1.5$ (where S_ν is the flux density at frequency ν in GHz) and $S_{217} < S_{353}$. Thirdly, we inspect each source with respect to the NASA/IPAC Extragalactic Database (NED), *IRAS* maps (Neugebauer et al. 1984), and optical maps using ALADIN. Any object identified as a local galaxy, a bright radio source or Galactic cirrus is removed (about half of the objects). Finally, we remove any PCCS source already falling in the H-ATLAS or South Pole Telescope (SPT) survey fields.

2.2. The *Planck* parent sample and three subsamples

Planck and *Herschel* were launched on 14 May 2009, and started routine scientific observations a few months later (Planck Collaboration I 2011; Pilbratt et al. 2010). Our *Planck* parent sample has evolved with time as a function of the delivery of in-

ternal releases of the intensity maps (typically every 6 months). We thus built three samples: one for each main *Herschel* Open Time call for proposals (OT1 and OT2), and a last one for the *Herschel* ‘must-do’ DDT (Director’s Discretionary Time) observations (which we call HPASSS for *Herschel* and *Planck* All Sky Legacy Survey Snapshot). We requested only SPIRE data, as it is better optimized than PACS for the targeted redshift range. Our main goal was to identify the counterparts contributing to the *Planck*-HFI detections, hence the focus on rapid SPIRE follow-up of a maximum number of targets. Obtaining PACS observations would have enhanced the angular resolution and wavelength coverage, but for these short observations would not have resulted in further constraints in most cases.

The samples are summarized in Table 1, together with the map sizes and time per Astronomical Observation Request (AOR). The OT1 sample refers to the *Herschel* first call for Open Time observations in July 2010 (P.I.: L. Montier). The OT2 sample refers to the *Herschel* second call for Open Time observations in September 2011 (P.I.: H. Dole). Figs. 1 and 2 show examples of this observation strategy. The *Herschel* and *Planck* All-Sky Source Snapshot Legacy Survey (HPASSS) was set up by the *Planck* collaboration (P.I.: H. Dole) in the response to ‘must-do’ DDT programme in June 2012. At that time, the preliminary PCCS was internally released to the collaboration, and we could benefit from the unique and timely *Herschel* and *Planck* synergy when the *Planck* products were approaching their final state and when *Herschel* surveys already demonstrated the efficiency of the SPIRE observations. We note that the SPIRE data from 9 *Planck* fields included in the HPASSS sample are *Herschel* archival data: 4C24.28-1 (program: OT2_rhuub_2); NGP_v1, NGP_h1, NGP_h2, SGP_sm3-h, GAMA12_rn1, NGP_v8, NGP_h6 (KPOT_seales01_2); Lockman_SWIRE.offset_1-1 (SDP_soliver_3); and Spider-1 – (OT1_mmiville_2).

2.3. SPIRE data processing, total SPIRE sample and definition of IN and OUT *Planck* regions

The SPIRE data were processed starting with ‘Level 0’ using HIPE 10.0 (Ott 2010) and the calibration tree ‘spire_cal_10_1’ using the Destriper module⁴ as mapmaker (baselines are removed thanks to an optimum fit between all timelines) for most observations. For 33 AORs, we had also to remove some particularly noisy detectors (PSWB5, PSWF8, and PSWE9 affected for Operational Days 1304 and 1305) from the Level 1 timelines. In that case, we processed the data with the naive scan mapper using a median baseline removal (the destriper module worked with all bolometers in Level 1). Turnarounds have been taken into account in the processed data. The useable sky surface area is thus extended, and goes beyond the nominal $7' \times 7'$ or $15' \times 15'$ as specified in the AORs (Table 1). Since we are close to the confusion limit, we included a check to confirm that the non-uniform coverage imposed by including the edges does not change the source detection statistics.

We have a total of 234 SPIRE targets. Of these, two fields were repeated observations, and have been used to check the robustness of our detections. Four fields from the PCCS appear as cirrus structures: diffuse, extended submillimetre emission without noticeable point sources. These fields were removed from the sample. This means that four out of 234 fields (1.7%) were contaminated by Galactic cirrus. The success rate of avoiding Galactic cirrus features is thus larger than 98%, thanks to our

Table 2. SPIRE 1σ total noise (instrument + confusion) levels measured in various fields, in mJy. Our *Planck* fields are denoted ‘*Planck* high- z ’.

Field	1σ noise level		
	250 μm	350 μm	500 μm
<i>Planck</i> high- z	9.9	9.3	10.7
HerMES Lockman-SWIRE	10.1	10.5	12.0
HLS	14.1	12.6	14.2

careful selection on the *Planck* maps of the cleanest 35% of the sky.

Our final sample thus contains 228 fields (i.e., 234 minus two repeated fields minus four cirrus-dominated fields). They are composed of (See Table 1): 10 sources from OT1; 70 sources from OT2; 124 objects from HPASSS CIB; and 24 sources from HPASSS PCCS.

Each SPIRE field of a *Planck* target is then separated into two zones: IN and OUT of the *Planck* source at 545 GHz (the frequency where our selection brings the best S/N ratio). The IN region boundary is defined as the 50% *Planck* intensity contour, i.e., the isocontour corresponding to 50% of the peak *Planck* flux, and encompasses the *Planck*-HFI beam. The OUT region is defined to be outside this region (see the thick white contours in Figs. 1 and 2).

2.4. Ancillary SPIRE data sets

For a first characterization of our sample, and to infer whether it is different from other samples of distant galaxies observed with SPIRE, we will compare with the data obtained in other SPIRE programmes. Since we suspect that most of our targets contain overdensities like proto-clusters of galaxies, it will be useful to contrast it with samples of galaxy clusters at lower redshift, as well as against blank fields. Our two comparison samples are as follows.

1. The HerMES⁵ (Oliver et al. 2010) and H-ATLAS⁶ (Eales et al. 2010) public data as reference fields. In particular, we will be using the ‘level 5’ Lockman HerMES field, which has a similar depth to our SPIRE observations.
2. The SPIRE snapshot programme of local or massive galaxy clusters (Egami et al. 2010) including: the ‘‘Herschel Lensing Survey’’ (HLS); the ‘‘SPIRE Snapshot Survey of Massive Galaxy Clusters’’ (OT1); and the ‘‘SPIRE Snapshot Survey II, Using SPT/CODEX Massive Clusters as Powerful Gravitational Lenses’’ (OT2)⁷.

Finally, we use the OT2 data from ‘‘The highest redshift strongly lensed dusty star-forming galaxies’’ (P.I. J. Vieira) programme to carry out technical checks, since those AORs are very similar to ours.

⁵ <http://hedam.oamp.fr/HerMES/>

⁶ <http://www.h-atlas.org/>

⁷ *Herschel* public data can be downloaded from the *Herschel* Science Archive: http://herschel.esac.esa.int/Science_Archive.shtml

⁴ Scan map destriper details: <https://nhscsci.ipac.caltech.edu>

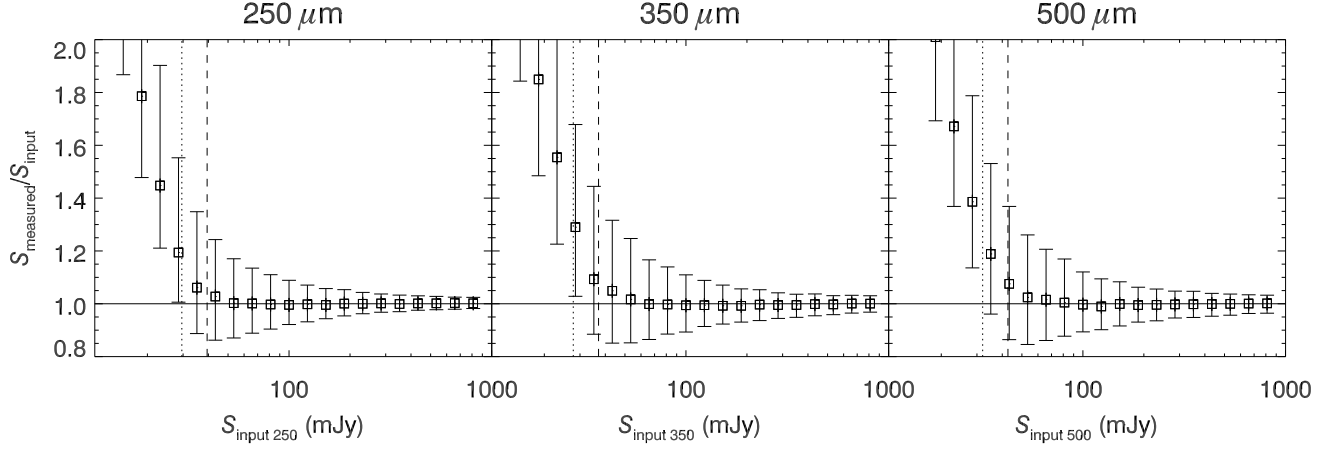


Figure 3. Photometric accuracy from Monte Carlo source injections in real maps at 250, 350 and 500 μm . The 3σ (dotted line) and 4σ (dashed line) levels are also shown. See Sect. 3.2 for details.

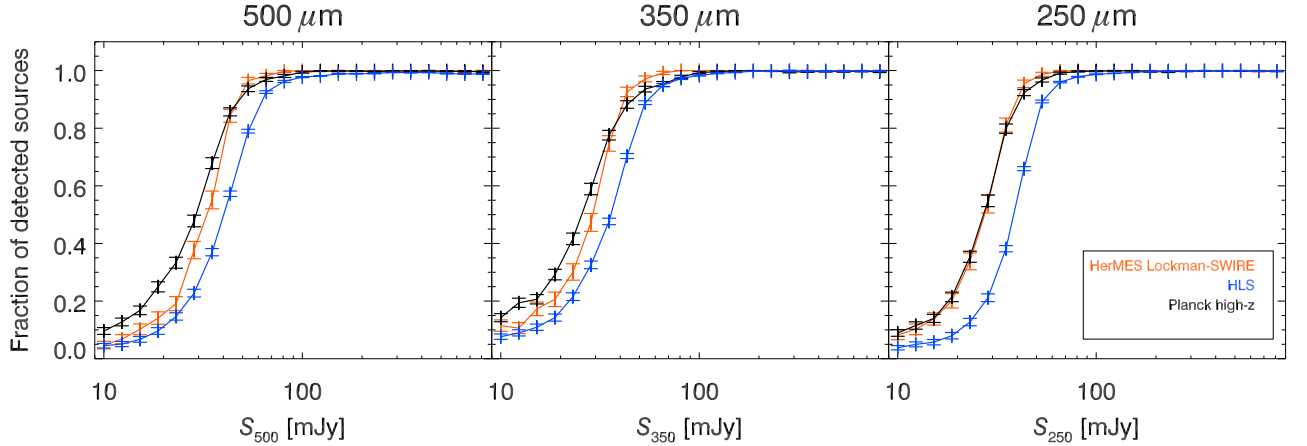


Figure 4. Completeness levels from Monte Carlo source injections in SPIRE maps of different data sets at 250, 350 and 500 μm . Plotted are our *Planck* fields (black), HerMES sources (orange), and Herschel Lensing Survey (HLS) clusters (blue). The 50% (dotted line) and 80% (dashed line) completeness levels are also shown. See Sect. 3.2 for details.

3. SPIRE Photometry

3.1. Photometric analysis

We first measure the noise in each map at each wavelength (channel) by fitting a Gaussian function to the histogram of the maps and deriving the standard deviation, σ_{channel} , a mixture of confusion noise (Dole et al. 2003; Nguyen et al. 2010) and detector noise. The values are reported in Table 2. Data are sky subtracted and at mean 0, as done in HIPE 10. All pixels are used to plot the noise histogram. Histograms have a Gaussian shape, with a bright pixel tail. The bright pixel tail contribution (larger than 3σ) to the histogram is nearly 1% in number for each field at 350 μm . Then we extract the sources using a blind method and by a band-merging procedure described in the following sections.

3.2. Blind catalogues

We detect blindly, i.e., independently at each frequency, the sources using StarFinder (Diolaiti et al. 2000). We use Gaussian point spread functions (PSFs) with FWHM of $18.15''$ for 250 μm , $25.15''$ for 350 μm , and $36.3''$ for 500 μm ⁸. These

⁸ for nominal SPIRE map pixels of 6, 10, and $14''$, respectively.

individual band catalogues are used for checking photometric accuracy and completeness, and to produce number count estimates. The catalogues are then band-merged in order to quantify the colours of the sources.

We employ Monte Carlo simulations to check our photometry at each wavelength: injection of sources in the data, and blind extraction, in order to measure the photometric accuracy (Fig. 3). As expected, the photometric accuracy is of the order of 10% at flux densities larger than a few tens of mJy, and decreases towards smaller flux densities closer to our noise level (dominated by confusion) at around 30 mJy. The completeness levels are also measured, and reported in Fig. 4 and Table 3.

3.3. Band-merged catalogues

We use the 350 μm map-based catalogue from StarFinder as the input catalogue. This wavelength has two advantages: first, its angular resolution meets our need to identify the sources; and second, it is consistent with the *Planck* colour selection, which avoids the many low- z galaxies peaking at 250 μm . As will be shown in Sect. 4.1, our sample has an excess in number at 350 μm compared to reference samples drawn from the HerMES Lockman SWIRE level 5 field or the low-redshift HLS

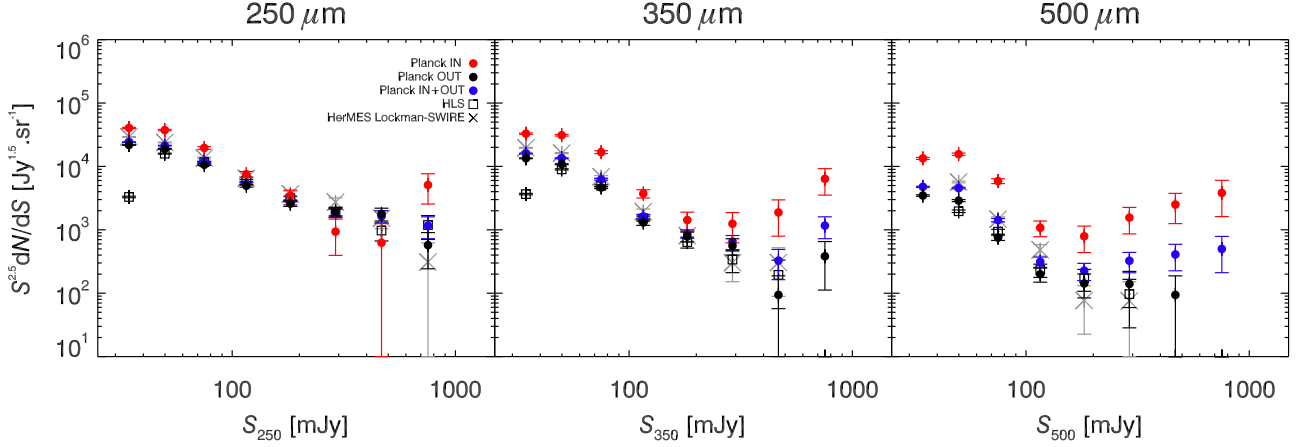


Figure 5. Differential Euclidean-normalized number counts, $S^{2.5}dN/dS$, for various data sets (not corrected for flux-boosting or incompleteness) used to measure the relative behaviour. Symbols show: *Planck* IN region (red circles, 228 fields); *Planck* OUT regions (black circles); *Planck* whole field, i.e., IN+OUT (blue circles); sample of 535 $z < 1$ clusters of the HLS (open square); and HerMES Lockman SWIRE blank field (crosses). Our SPIRE sources corresponding to the *Planck* IN regions clearly show an excess in number density at 350 and 500 μm , illustrating their red colour, and a potentially higher redshift than average. See Sect. 4.1 for details.

Table 3. 80% completeness levels obtained from Monte Carlo source injection in the SPIRE maps for different fields, in mJy. Our *Planck* fields are denoted “*Planck* high- z ”.

Field	80% Completeness		
	250 μm	350 μm	500 μm
<i>Planck</i> high- z	35.2	37.0	40.7
HerMES Lockman-SWIRE	35.0	38.4	42.7
HLS	49.3	48.5	54.3

cluster fields, in agreement with the existence of an overdensity of SPIRE sources in the *Planck* beam.

Our band-merging procedure has three steps. First of all, we optimize the measurement of the source position using the 250 μm channel, where available. Secondly, we measure a preliminary flux density on each source, which will serve as a prior to avoid unrealistic flux measurements while deblending. Thirdly, we perform spatially-simultaneous PSF-fitting and deblending at the best measured positions with the newly determined prior flux densities as inputs for FastPhot (Bethérmin et al. 2010b). The details are described in Appendix A. This method provides better matched statistics (more than 90% identifications) than the blind extraction method performed independently at each wavelength (Sect. 3.2, Table A.2 vs. Table A.1). We finally have a total of about 7100 SPIRE sources, of which about 2200 are located in the *Planck* IN regions (giving an average of about 10 SPIRE sources per *Planck* IN field).

4. Statistical Analysis of the Sample

4.1. Number counts: significant excess of red sources

We compute the differential Euclidean-normalized number counts $S^{2.5}dN/dS$, with S being the flux density at wavelength λ , and N the number of sources per steradian. The counts are not corrected here for incompleteness, or for flux boosting (Eddington bias), since we are interested in the relative be-

haviour between the samples. The detected sources used here are extracted using the blind technique (Sect. 3.2). We cut the samples at 4σ for these counts (σ values in Table 2). We used five different data sets to estimate the number counts:

- *Planck* IN+OUT, our 228 *Planck* entire fields, each covering about $20' \times 20'$;
- *Planck* IN, our 228 *Planck* fields, using only the central parts corresponding to the *Planck* 50% contour level (determined separately for each source), called the IN region;
- *Planck* OUT, our 228 *Planck* fields, using only the part exterior to the *Planck* 50% level, called the OUT region;
- HerMES Lockman SWIRE, HerMES level 5 field in Lockman (Oliver et al. 2010), covering 18.2 deg^2 ;
- HLS, 535 cluster-fields of Egami et al. (2010), five from the Herschel Lens Survey KPOT, 282 from OT1, and 248 from OT2, hereafter referred to as HLS.

The number counts of all these data sets are plotted in Fig. 5 and reported in Appendix B in Tables B.1, B.2, and B.3. We derive from the total number count the following results.

- The counts measured in the entire *Planck* fields (blue circles, meaning IN + OUT), HerMES Lockman, and HLS clusters, are generally compatible with each other at 250 μm , except for a few points at large flux density, above 300 mJy, where the numbers are small. This means that, on average, those fields do not show any strong deviations between them.
- The observed counts (uncorrected for incompleteness) show the characteristic shape of the Eddington bias: a cut-off below about 40 mJy, an excess around 50 mJy, and a behaviour compatible with the models at higher flux densities. It is beyond the scope of this paper to re-derive unbiased number counts (e.g., Glenn et al. 2010; Oliver et al. 2010; Clements et al. 2010), as we only focus on the relative trends.
- The IN counts at large flux densities ($S > 300 \text{ mJy}$) show a systematic excess at 350 and 500 μm over the counts in the wide blank field (Lockman) as well as cluster fields. At 300 mJy, the overdensity factors are, respectively, 4.1 and

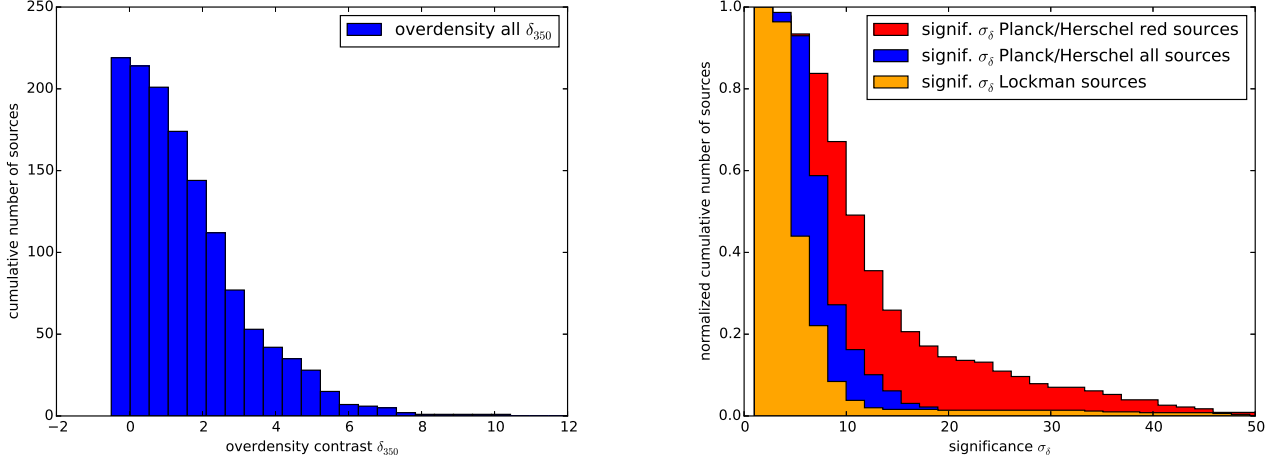


Figure 6. *Left:* Cumulative histogram of the overdensity contrast δ_{350} (blue) of each *Planck* field (based on $350\ \mu\text{m}$ SPIRE sources). Overdensities are fairly large, with 59 fields having $\delta_{350} > 3$. *Right:* Cumulative (normalized) statistical significance in σ derived from the density maps. Blue represents all our SPIRE sources, red represents only redder SPIRE sources, defined by $S_{350}/S_{250} > 0.7$ and $S_{500}/S_{350} > 0.6$, and orange 500 random fields in Lockman. Most of our fields have a significance greater than 4σ , and the significance is higher still for the redder sources. See Sect. 4.2 for details.

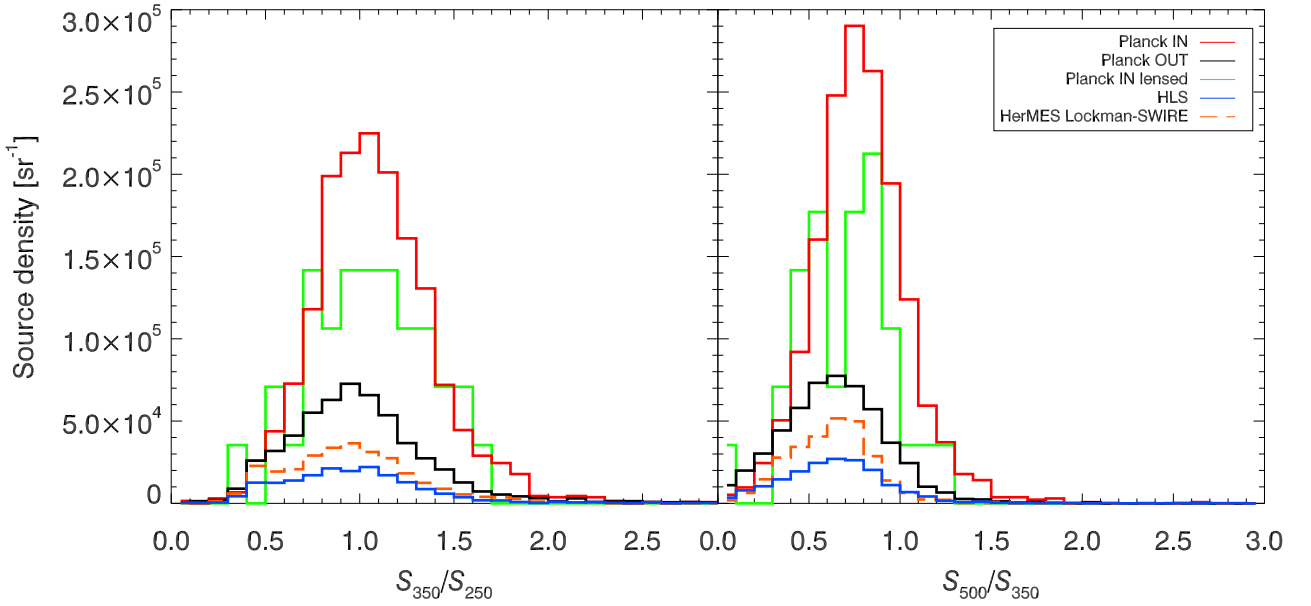


Figure 7. Colour counts: source surface density as a function of the SPIRE colour, S_{350}/S_{250} (left), and S_{500}/S_{350} (right). Histograms are: red solid line, *Planck* IN; black line, *Planck* OUT; green, *Planck* IN lensed fields only; blue line, $z < 1$ HLS clusters; and orange dashes, Lockman SWIRE. The *Planck* IN sources (total and/or lensed sources) show a much higher surface density than other samples, owing mainly to our all-sky search strategy. See Sect. 4.3 for details.

3.7 at $350\ \mu\text{m}$, and about 20 and 16 at $500\ \mu\text{m}$. This chromatic excess (i.e., larger excess at longer wavelengths) is consistent with the hypothesis of the presence of a population of high-redshift lensed candidates at $z = 2-4$. We will show in Sect. 5 that this is indeed the case.

(iv) The IN counts at $250\ \mu\text{m}$ are a bit higher (for $S_{250} < 100\ \text{mJy}$) than in Lockman, and are lower at larger flux densities. This means that the SPIRE counterparts of the *Planck* sources have, on average, counts that deviate little from blank fields at this wavelength.

(v) The IN counts at $350\ \mu\text{m}$ for $S_{350} \approx 50\ \text{mJy}$ are a factor between 1.9 and 3.4 higher than in Lockman and in the cluster fields. This means that, on average, the SPIRE counterparts of the *Planck* sources have a significant excess of $350\ \mu\text{m}$ sources compared to wide blank fields or $z < 1$ HLS cluster fields. This is expected, given our *Planck* selection criteria.

(vi) The IN counts at $500\ \mu\text{m}$ for $S_{500} \approx 50\ \text{mJy}$ are a factor of 2.7–8 higher than in the Lockman and cluster fields. As in item (v) above, this means that, on average, the SPIRE images of the *Planck* source targets show a significant excess

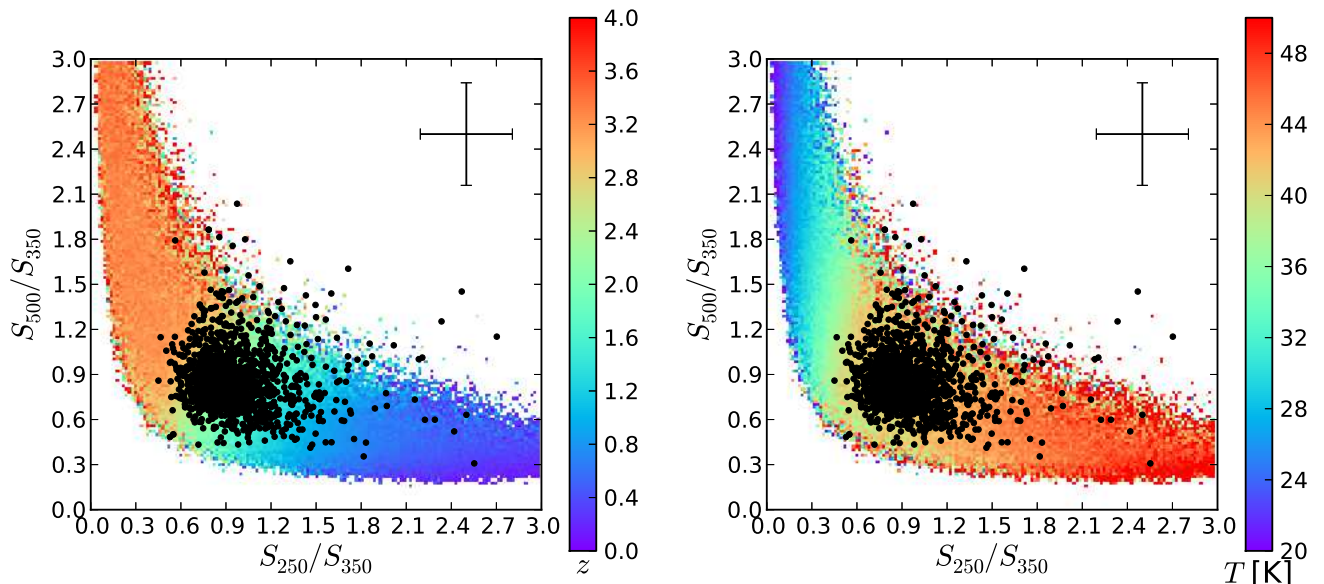


Figure 8. *Herschel*-SPIRE colour-colour diagram of IN sources (black dots) on top of redshifted blackbodies. *Left*: colour codes redshift. *Right*: colour codes dust temperature in kelvin. Although there is a degeneracy between redshift and temperature, the colours suggest a range of $z \sim 1.5\text{--}3$ for the SPIRE sources corresponding to the *Planck* IN regions. The upper right symbol gives the typical (median) error bars of the measured points. See Sect. 4.3 for details.

of $500\mu\text{m}$ sources compared to wide blank field or $z < 1$ HLS cluster fields.

- (vii) The OUT counts are compatible with the wide blank extragalactic fields, as well as the cluster fields. Our OUT zones can thus also be used as a proxy for the same statistics in blank fields.

As a conclusion, the SPIRE observations of the *Planck* fields reveal “red” sources. The SPIRE images exhibit a significant excess of 350 and $500\mu\text{m}$ sources in number density compared with wide blank fields (HerMES Lockman SWIRE of the same depth) or fields targeting $z < 1$ galaxy clusters (HLS). This significant excess should be expected given the *Planck* colour selection, and is now demonstrated with secure SPIRE detections. It is therefore clear that there is no significant contamination by cirrus confusion in our *Planck* sample, and that where there is a *Planck* high- z candidate, *Herschel* detects galaxies.

4.2. Overdensities

We compute the dimensionless overdensity contrast δ_λ of our fields at wavelength λ via

$$\delta_\lambda = \frac{\rho_{\text{IN}} - \rho_{\text{OUT}}}{\rho_{\text{OUT}}}, \quad (1)$$

where ρ_{IN} is the surface density of SPIRE sources in the *Planck* IN region, and ρ_{OUT} is the mean surface density of SPIRE sources computed in the *Planck* OUT region, at SPIRE wavelength λ . We have already shown (Sect. 4.1 and Fig. 5) that the OUT region has a density equivalent to that of blind surveys, and is thus a good estimate of $\bar{\rho}$, the mean surface density. To reduce the Poisson noise, we use the counts from *all* the OUT regions.

The overdensity contrasts δ_λ extend up to 10, 12, and 50 at 250 , 350 , and $500\mu\text{m}$, respectively, with a median overdensity δ_λ of $\delta_{250} = 0.9$, $\delta_{350} = 2.1$, and $\delta_{500} = 5.0$. This means that our *Planck* IN regions have an excess of SPIRE sources. Indeed, there are 50 fields with $\delta_{500} > 10$, and 129 with $\delta_{500} > 4$

(with significance levels always higher than $4\sigma_\delta$, see below). At $350\mu\text{m}$, there are 19 fields with $\delta_{350} > 5$, 37 fields with $\delta_{350} > 4$ and 59 fields with $\delta_{350} > 3$, as shown in Fig. 6 (left panel, in blue). In Appendix D, we also use the densities measured with AKDE to estimate the overdensities.

How significant are these overdensity contrasts? To quantify this we compute the mean density field using the AKDE algorithm (adaptive kernel density estimator, see Valtchanov et al. 2013 and also Pisani 1996; Ferdosi et al. 2011). The principle is to generate a two-dimensional density field based on the positions of the sources from a catalogue, filtered (smoothed) according to the source surface density. From this smoothed field, we compute the standard deviation and hence we derive the significance σ_δ of the overdensity. We also run 1000 Monte Carlo runs to get a better estimate of the scatter on σ_δ (by creating AKDE density maps using random source positions – but otherwise using the real catalogs of each field – and measuring the RMS over those 228000 realizations). All our fields show overdensities larger than $1.8\sigma_\delta$, with a median of $7\sigma_\delta$ (Fig. 6 right panel). The typical number of sources in an overdensity is around 10, but with a fairly wide scatter.

We can then choose to select the reddest sources, this being a possible signature of a higher redshift or a colder dust temperature. We define the SPIRE red sources with the following cuts in colour based on the distributions shown in Fig. 7: $S_{350}/S_{250} > 0.7$; and $S_{500}/S_{350} > 0.6$. When selecting only the red sources, the overdensity significance increases: The mean is now $12\sigma_\delta$ and the median $9\sigma_\delta$. We have 50% of the sample at $10\sigma_\delta$ or more (when selecting the red sources), which is more than a factor of 3 larger than when selecting all SPIRE sources. 23% of the sample is above $15\sigma_\delta$ (Fig. 6 right panel), i.e., 51 fields.

These high significance levels can be contrasted with the mean $\delta_{500} \approx 0.25$ obtained by Rigby et al. (2014) at the locations of 26 known protoclusters around very powerful radiogalaxies, drawn from the list of 178 radiogalaxies at $z > 2$ of Miley & de Breuck (2008). They can also be compared to the few similar ex-

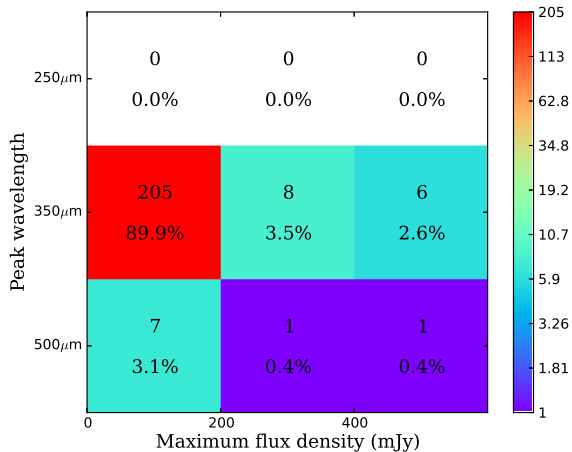


Figure 9. Classification of 228 *Planck* fields with *Herschel*-SPIRE. The x -axis represents the maximum flux of the SPIRE source within the IN region: lensed source candidates are selected if they fall above 400 mJy (i.e., the right column, seven sources). The y -axis represents the wavelength at which the brightest SPIRE source peaks in the IN region. Overdensities are thus selected in the lower left four cells. The colour represents the number of fields in each cell (as shown in the colour bar), the numbers in the cells are the number of fields and percentage in each cell. Our sample is thus dominated by overdensities peaking at 350 μm . See Sect. 4.4 for details.

amples in Clements et al. (2014), with at most $4.7 \sigma_\delta$ at 350 μm . We show in Fig. 6 right panel, in orange, the cumulative normalized significance σ_δ of 500 random positions in the Lockman field; Using this test sample illustrates the high significance of the overdensities of our sample.

Examples of some overdensities are shown in Appendix E, where we present a gallery of representative SPIRE data.

4.3. Colours of the sources

Using the band-merged catalogue (Sect. 3.3), we can derive the colours of the sources, i.e., the ratios of the observed flux densities S_{500}/S_{350} vs. S_{250}/S_{350} . In this colour-colour space, redder sources will have higher S_{500}/S_{350} ratios and lower S_{250}/S_{350} ratios, and will tend to lie in the lower left part of the diagram.

We provide in Fig. 7 the source surface density histograms for the two SPIRE colours: S_{350}/S_{250} and S_{500}/S_{350} (red, *Planck* IN; black, *Planck* OUT; green, only the lensed fields; blue, HLS; and dashes, HerMES). The IN sources show three times larger surface densities in S_{350}/S_{250} , and four times larger surface densities in S_{500}/S_{350} than OUT and Lockman sources. The IN source distribution peaks at much higher surface density than any other sample, suggesting that our sample is dominated by red and overdense SPIRE sources.

Following the approach of Amblard et al. (2010), we generate the SED of 10^6 modified blackbodies with 10% Gaussian noise and explore three parameters: the blackbody temperature (T) in the range 10–60 K; the emissivity (β) in the range 0–2; and the redshift for $z = 0$ –5. For each set of parameters we convert the fixed, observed SPIRE wavelengths into rest frame wavelength (at redshift z , thus varying with z) using: $\lambda_{\text{rest}} = \lambda_{\text{SPIRE}}/(1+z)$. We then calculate the flux at each wavelength using λ_{rest} and compute the colours S_{250}/S_{350} and S_{500}/S_{350} for

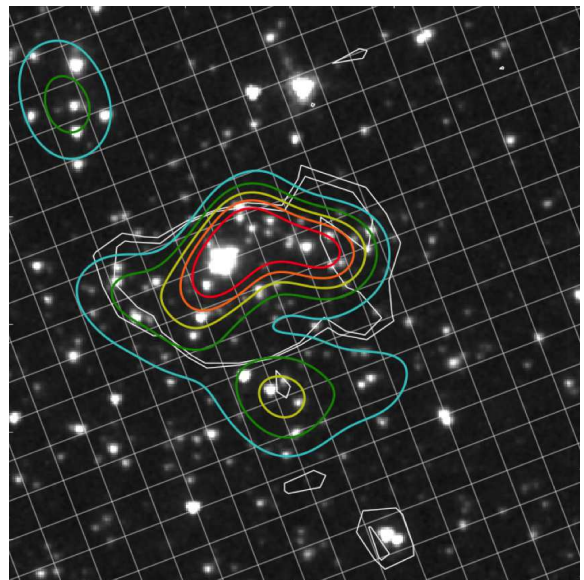


Figure 10. A high- z cluster candidate observed by *Planck*, *Herschel*, and *Spitzer*-IRAC (image covering $0.5' \times 0.3'$). We show the IRAC channel 1 (3.6 μm) image, with SPIRE 350 μm white contours overlaid. Colour contours represent statistical significance of the local overdensity, from light blue to red: 3, 4, 5, 6, and $7 \sigma_\delta$. See Sect. 6.1 for details.

each set of parameters. Fig. 8 shows those realizations, colour-coded in redshift (deep purple for $z = 0$, up to red for $z = 4$). Our SPIRE IN sources are shown in black. They predominantly fall in the redshift region corresponding to $z \sim 1.5 - 3$. We note, however, that the redshift-temperature degeneracy is present in this suggestive result (Amblard et al. 2010; Pope & Chary 2010; Greve et al. 2012), and will be discussed in Sect. 6.3.

4.4. Classification of the sources

We classify the *Herschel* fields in an automated way and for preliminary analysis into two main categories: (1) *overdensities*, appearing as clustered sources, and (2) *lensed candidates*, appearing as a bright single source as a counterpart of the *Planck* source. To make this classification, we measure within the IN *Planck* region the flux density and colour of the brightest SPIRE source.

We sort the fields using two criteria: (1) the SPIRE channel at which the source has its maximum flux density; and (2) its flux density at 350 μm . We will use this two-parameter space to classify the sources. This classification provides the first set of information about the sources, although a definitive classification will require follow-up data to confirm the nature of the sources.

In this space, the lensed candidates will populate the “red” and “bright” areas (typically 350 or 500 μm peakers, and $S_\nu > 400$ mJy). This does not necessarily mean that all the sources in this area will be strongly gravitationally lensed (although this is confirmed by further follow-up, see following sections).

The overdensity candidates will be located in a different area of this two-parameter space than the lensed candidates. They will tend to populate the fainter end (typically $S_\nu < 200$ mJy) and will have red colours (typically 350 or 500 μm peakers).

We do not expect many 250 μm peakers because of the *Planck* colour selection, for which there is a bias towards redder colours and thus potentially higher-redshift sources.

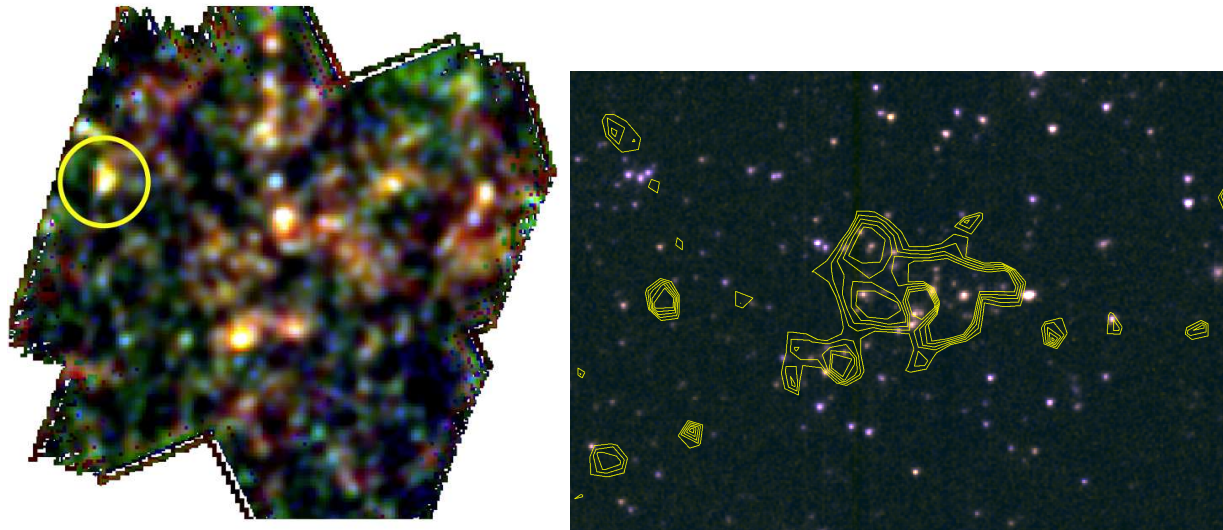


Figure 11. *Left:* SPIRE 3-colour image of one *Planck* high- z overdensity candidate (located in the centre), in an image covering about $20' \times 20'$. We note the bluer source on the left (circled), which corresponds to the galaxy cluster shown on the right. *Right:* a confirmed $z = 1.58$ galaxy cluster XMMU J0044.0-2033 (Santos et al. 2011) which lies close to our *Planck* high- z source. The background image is a two colour composite of *Spitzer*-IRAC channel 1 ($3.6 \mu\text{m}$) and channel 2 ($4.5 \mu\text{m}$), covering about $3' \times 2'$. The contours are *Herschel*-SPIRE $350 \mu\text{m}$. See Sect. 6.1 for details.

Fig. 9 summarizes the classes of SPIRE identifications of the *Planck* high- z (meaning $z > 1.5$) candidates, based on those criteria. We show that the vast majority of our sample is composed of overdensities of $350 \mu\text{m}$ peakers. The number of lensed candidates is rather small in comparison, amounting to seven sources based on this criterion. All are confirmed to be strongly gravitationally lensed galaxies (Canameras 2015). We will show later that visual inspection led us to discover a few more lensed sources.

The dashed lines in Fig. 7 show the colour vs. surface density of the lensed candidate population, whose red colours are confirmed.

Finally, we derived number counts (as in Fig. 5) but now by separating the overdensities from the lensed sources that dominate the counts at large flux densities, typically $S > 250 \text{ mJy}$ (shown in Appendix C in Fig. C.1). This separation suggests that the excess at large flux densities in the number counts of our sample is due to the presence of bright lensed sources, compared to reference samples (HLS, HerMES).

5. Strongly gravitationally lensed source candidates

5.1. Validation of existing lensed sources

Negrello et al. (2007) and Bethermin et al. (2012) predicted that a small, but significant fraction of very bright high-redshift ($z > 2$) submillimetre galaxies are strongly gravitationally lensed, dusty starbursts in the early Universe. Negrello et al. (2010) presented observational evidence of these predictions. In addition, Fu et al. (2012) confirmed the nature of the source H-ATLAS J114637.9-001132 as a strongly gravitationally lensed galaxy at $z = 3.3$; this source was part of the first release of the *Planck* ERCSC Catalogue (Planck Collaboration VII 2011; Planck Collaboration 2011), and fell fortuitously into the H-ATLAS survey field (see also Herranz et al. 2013). Another independent confirmation that *Planck* sources can be strongly gravitationally lensed came from the source HLS J091828.6+514223,

confirmed as a bright, $z = 5.2$ gravitationally lensed galaxy behind the massive intermediate-redshift galaxy cluster Abell 773 (Combes et al. 2012), as part of the *Herschel* Lensing Survey (Egami et al. 2010). This source was independently found in our survey and is part of the *Herschel*/SPIRE OT2 selection. It is excluded from our sample to satisfy the condition of non-redundancy.

5.2. Previously unknown gravitationally lensed sources

In the absence of extensive follow-up, it is challenging to distinguish between single or multiple strongly gravitationally lensed galaxies behind the same foreground structure and overdensities of intrinsically bright submillimetre galaxies, for all but the brightest gravitationally lensed sources. Moreover, at flux densities of about $S_{350} = 250 \text{ mJy}$ and above, isolated SPIRE point sources may turn out to be associations of multiple FIR galaxies when observed at higher spatial resolution (Iverson et al. 2013).

As a first step towards identifying the gravitational lensed candidates in our sample (Sect. 4.4), we therefore focused on those targets where SPIRE shows only a single, very bright source, with the typical FIR colours of high-redshift ($z > 2$) galaxies associated within one *Planck* beam. We thus identified seven isolated SPIRE point sources, as described in Sect. 4.4, plus five others at slightly fainter flux densities. All have peak flux densities at $350 \mu\text{m}$, including 11 with $S_{350} = 300\text{--}1120 \text{ mJy}$ (Canameras 2015). Six of these galaxies were taken from the PCCS, the remaining six originate from the sample of Planck Collaboration (2015). Although the initial selection of lensed candidates was carried out by eye upon the reception of the SPIRE imaging, seven of these targets were also identified with our automatic classification (Sect. 4.4). We used the IRAM 30-m telescope to obtain firm spectroscopic redshifts via a blind CO line survey with the wide-band receiver EMIR. We identify 2–6 lines per source, which confirms they are at redshifts $z = 2.2\text{--}3.6$. Interferometry obtained with the IRAM Plateau de Bure interferometer and the Submillimeter Array, as well as several empirical calibrations based on FIR luminosity and dust

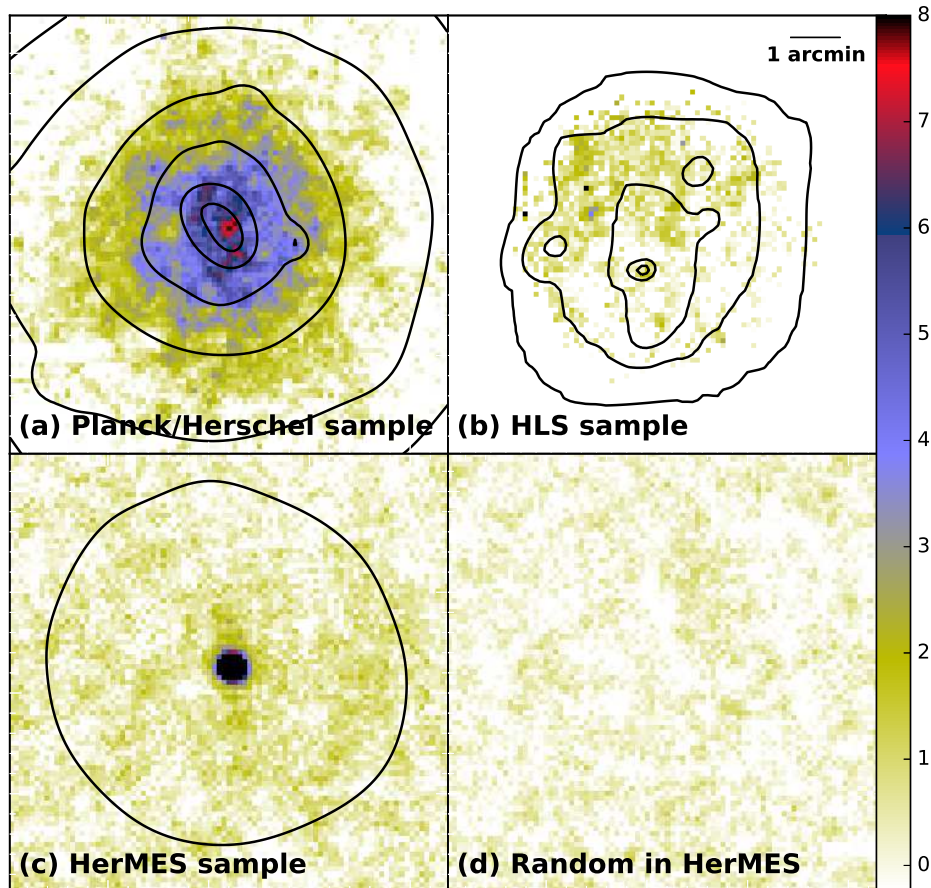


Figure 12. Stacks of SPIRE $350\ \mu\text{m}$ data ($8.7' \times 8.7'$): (a) 220 *Planck Herschel* fields; (b) 278 HLS clusters; (c) 500 sources in the HerMES Lockman field, peaking at $350\ \mu\text{m}$; and (d) 500 random positions in the HerMES Lockman field. Black contours show the density of red sources (using AKDE). Our *Planck* fields clearly exhibit a high significance of extended (a few arcminutes) submm emission, due to the presence of many red point sources, not seen in the HLS or HerMES sources. See Sect. 6.2 for details.

temperature (following Harris et al. 2012), and CO line luminosity and line width (following Greve et al. 2012), demonstrate that these are indeed strongly gravitationally lensed galaxies, amongst the brightest on the submm sky (Canameras 2015).

6. Candidate high- z overdensities

Without rejecting the possibility that the observed overdensities of red SPIRE sources could be chance alignments of structures giving coherent colours (e.g., Chiang et al. 2013), we can ponder the nature of those overdensities. Could they be high-redshift intensively star-forming galaxy proto-clusters? Indeed, recent studies, such as Gobat et al. (2011), Santos et al. (2011, 2013, 2014), and Clements et al. (2014) confirm the presence of high redshift ($z > 1.5$) galaxy clusters emitting enough energy in the submillimetre to be detected. Those previously detected clusters are, however, in a different state of evolution than our candidates. Many of the confirmed clusters exhibit X-ray emission, suggesting already mature and massive clusters. The following sections investigate different aspects of our sample, which is uniquely selected by strong submm emission over the whole sky, enabling us to unveil a rare population.

6.1. First confirmations

It is beyond the scope of this paper to summarize all the follow-up observations conducted so far, but we give here three high-lights, which will be discussed in more detail in subsequent papers.

Our sample contains a source from *Herschel* OT1 that was followed up early as a pilot programme. Using CFHT and *Spitzer* imaging data, and VLT and Keck spectroscopy, a structure was identified at $z \sim 1.7\text{--}2.0$ (Flores-Cacho et al., 2014, in prep.). By fitting a modified blackbody and fixing redshifts at respectively 1.7 and 2.0, we find an average dust temperature for the sources of, respectively, 27K and 35K.

Another field has been imaged by *Spitzer* as part of our GO-9 programme – see Fig. 10 for the IRAC $3.6\ \mu\text{m}$ image with the SPIRE $350\ \mu\text{m}$ contour. The colour ratios of IRAC flux densities $3.6\ \mu\text{m}/4.5\ \mu\text{m}$ of the sources detected in the overdensity exhibit red colours, indicating their probable high-redshift nature (Papovich 2008). The overdensity of IRAC $3.6\ \mu\text{m}$ sources has a statistical significance of $7\ \sigma_\delta$ (Martinache et al., 2014, in prep.). While not yet confirmed as a proto-cluster or cluster through spectroscopy, this structure, seen with *Spitzer* at near-infrared wavelengths, supports the hypothesis of strongly clustered highly star-forming infrared sources.

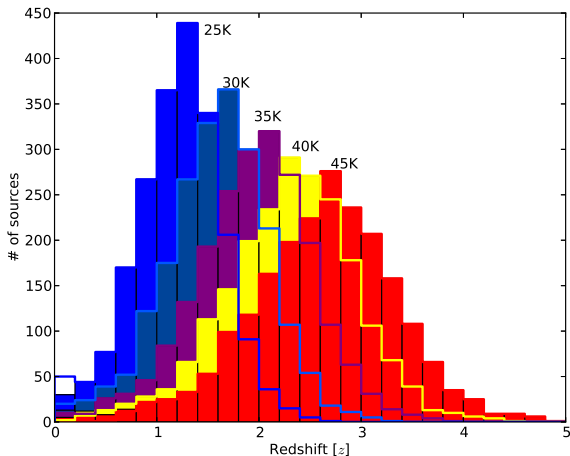


Figure 13. SPIRE photometric redshift distribution of the roughly 2200 SPIRE sources in the IN regions, as a function of the fixed assumption for dust temperature: $T_d = 25, 30, 35, 40,$ and 45 K (from left to right). See Sect. 6.3 for details.

Finally, we have also found one SPIRE field with overlapping data from the literature. The observations from Santos et al. (2011) confirm the presence of a $z = 1.58$ cluster using optical/NIR spectroscopy. This particular high- z cluster has also been detected in X-rays, leading to a total mass estimate of about $3\text{--}5 \times 10^{14} M_\odot$. It is located a few arcminutes from one of our targets (Fig. 11 right), so is not formally an identification of our *Planck* source, but rather a coincidence. While not connected to our target source here, this cluster can nevertheless bring useful information. The SPIRE colours of this cluster are bluer than our sources. Since our target shows redder SPIRE colours, this suggests it has a higher redshift or a cooler dust temperature.

6.2. Large clustering of our sample revealed with stacking

We can investigate if the observed overdensities have different clustering properties than two test samples: (1) the HLS massive $z < 1$ clusters; and (2) $350\ \mu\text{m}$ peaker sources in the HerMES Lockman field brighter than 50 mJy. To do so, we use a stacking analysis (see, e.g., Montier & Giard 2005; Dole et al. 2006; Braglia et al. 2011), here applying the method of Bethermin et al. (2010a). We stack the following SPIRE $350\ \mu\text{m}$ data: (a) the 220 overdensities of our sample; (b) 278 HLS clusters; (c) 500 bright $350\ \mu\text{m}$ peaker sources in the Lockman field; and (d) 500 random positions in the HerMES Lockman field as a null test. The stacks are presented in Fig. 12.

We can see that the *Planck* fields show clear and significant extended (a few arcminutes) emission due to the clustering of bright submm sources. This kind of extended emission of clustered submm sources is not observed in the HLS clusters, nor around $350\ \mu\text{m}$ peaking HerMES sources. The random stack validates the absence of a systematic effect in stacking (Dole et al. 2006; Bethermin et al. 2010a; Viero et al. 2013; Planck Collaboration XVIII 2014). This proves that our sources are of a different nature than mature HLS clusters or average HerMES submillimetre sources.

We overplot in Fig. 12 the contours in density (see Sect. 4.2) of the SPIRE red sources (defined in Sect. 4.2). The stacks indicate that the *Planck* sample exhibits strong overdensities of red

SPIRE sources. By contrast, the HLS sample shows a smooth and weak density of red sources (except for the presence of some point sources – the background lensed galaxies). As expected, the HerMES sample shows a stack consistent with the SPIRE PSF, while the random sample is consistent with noise.

6.3. Dust temperatures, photometric redshifts, luminosities, and star formation rates

With the hypothesis that our overdensities are actually gravitationally bound structures, i.e., clusters of star-forming, dusty galaxies, the overdensity colours (Fig. 7) suggest a peak redshift around $z = 1.5\text{--}3$ (Fig. 8). Using a modified blackbody fit (with $\beta = 1.5$) and fixing the dust temperatures to $T_d = 25, 30, 35, 40,$ and 45 K, we obtain the redshift distributions shown in Fig. 13 for the roughly 2200 sources found in the IN regions for these overdensities. For $T_d = 35$ K, the distribution peaks at $z = 2$. For higher dust temperatures, the peak of the distribution is shifted towards higher redshifts, since dust temperature and redshift are degenerate for a modified blackbody, where $T_d/(1+z) = \text{constant}$.

Many studies (e.g., Magdis et al. 2010; Elbaz et al. 2011; Greve et al. 2012; Magdis et al. 2012; Symeonidis et al. 2013; Weiss et al. 2013; Magnelli et al. 2014) suggest that dust temperatures of $z \sim 2$ sources are typically of the order of 35 K, consistent with the few measurements in hand (see Sect. 6.1). With the conservative assumption that $T_d = 35$ K for all sources (e.g., Greve et al. 2012), we can derive the IR luminosity for each SPIRE source (by integrating between $8\ \mu\text{m}$ and 1 mm), and find that it has a broad distribution peaking at $4 \times 10^{12} L_\odot$ (Fig. 14). Assuming that the conventionally assumed relationship between IR luminosity and star formation (Kennicutt 1998; Bell 2003) holds, and that AGN do not dominate (as was also found for the objects previously discussed by Santos et al. 2014 and Clements et al. 2014), this would translate into a peak SFR of $700 M_\odot \text{yr}^{-1}$ per SPIRE source (Fig. 15). If we were to use colder dust temperatures, the peak SFR would be at about $200 M_\odot \text{yr}^{-1}$ per SPIRE source (Fig. 15). If we were to use warmer dust temperatures, the SFR would increase because the implied redshift would be higher and still compatible with other observations, e.g., the compilation of submillimetre galaxies in Greve et al. (2012), where L_{IR} is measured in the range $3 \times 10^{12}\text{--}10^{14} L_\odot$ and T_d in the range $30\text{--}100$ K, for redshifts above 2.

We can also estimate the IR luminosities and SFRs of the overdensities, i.e., potential clusters of dusty galaxies at high- z , rather than the single SPIRE sources that we used above. With typically 10 SPIRE sources in the IN region, we sum up the IR luminosities of SPIRE sources within the IN region (under the same assumption of $T_d = 35$ K) to obtain a peak IR luminosity of $4 \times 10^{13} L_\odot$. This translates to a peak SFR of $7 \times 10^3 M_\odot \text{yr}^{-1}$ per structure, as seen in Fig. 16.

Our estimates of L_{IR} are within the range of FIR luminosities expected for massive, vigorously star-forming high- z structures (e.g., Brodwin et al. 2013), which are perhaps proto-clusters in their intense star formation phase, and are consistent with the four bound structures found in Clements et al. (2014). These $z > 2$ intensely star forming proto-clusters are also expected in some models, e.g., the proto-spheroids of Cai et al. (2013), or the halos harbouring intense star formation discussed in Bethermin et al. (2013).

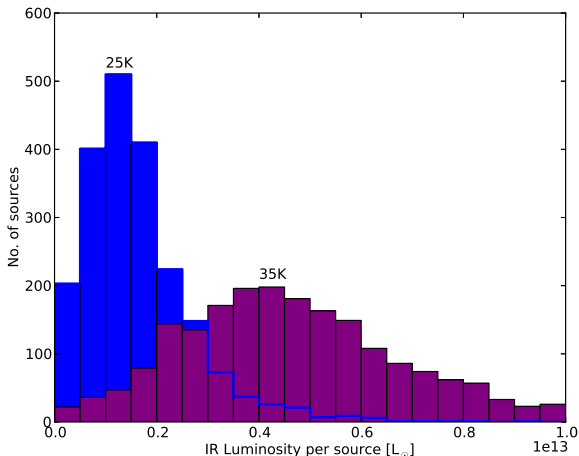


Figure 14. Infrared luminosities (L_{IR}) of the approximately 2200 SPIRE sources in the IN regions, as a function of the fixed dust temperature: 35 K (purple, right histogram), and also shown for illustration 25 K (blue, left histogram). See Sect. 6.3 for details.

6.4. Massive galaxy clusters in formation?

It is of course tempting to postulate that all (or at least a subset) of our sources include massive galaxy clusters in the process of formation. However, demonstrating this conclusively with the present *Herschel* photometry alone is not possible. We have therefore undertaken a comprehensive multi-wavelength photometric and spectroscopic follow-up campaign to directly constrain the nature of our sources and in particular, to investigate whether they are good candidates for being the progenitors of today’s massive galaxy clusters seen during their most rapid phase of baryon cooling and star formation.

Even without such an explicit analysis of the astrophysical nature of our candidates, we can already state that: (1) our estimated luminosities are consistent with the expected star formation properties of massive galaxy clusters, as obtained from stellar archaeology in galaxies in nearby clusters and out to redshifts $z \sim 1$; and (2) our total number of overdensities are consistent with the expected numbers of massive high- z galaxy clusters, as obtained from models of dark matter halo structure formation.

For point (1), a broad consensus has now been developed whereby most of the stellar mass in massive cluster galaxies was already in place by $z \approx 1$. The most stringent observational constraint is perhaps the tight red sequence of cluster galaxies in colour-magnitude diagrams of massive galaxy clusters in the optical and near-infrared (e.g., [Renzini 2006](#)), which suggests that massive cluster galaxies formed most of their stellar populations within a short timescale of ≤ 1 Gyr, i.e., within one cluster dynamical time, with little star formation thereafter. Rest-frame optical studies of distant clusters suggest that the bright end of the red sequence was already in place by $z \approx 1$ ([Rudnick et al. 2009](#)), with a likely onset amongst the most massive galaxies by ≈ 2 , or even before ([Kodama et al. 2007](#)).

The shortness of the star formation period in nearby clusters allows us to derive an order-of-magnitude estimate of the total star formation rates during this period, as implied by the fossil constraints, and the resulting FIR fluxes. To obtain upper limits on the stellar mass formed during this epoch, we use stellar mass estimates obtained for 93 massive X-ray-selected clusters

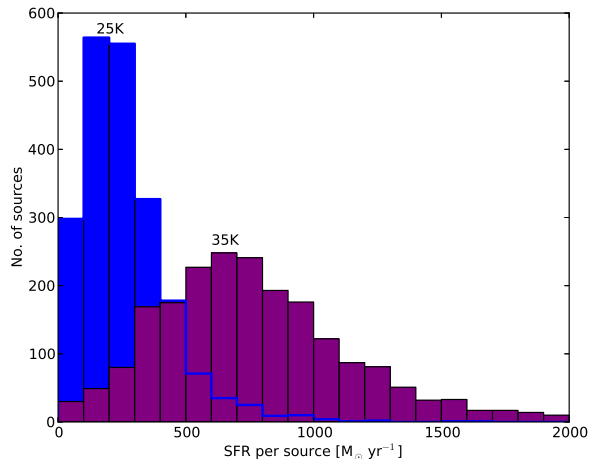


Figure 15. Star formation rate (SFR) for individual SPIRE sources in the overdensity sample (i.e., in the *Planck* IN region). For $T_d = 35$ K, a dust temperature favoured by the literature, (purple, right histogram) the distribution peaks at $700 M_{\odot} \text{ yr}^{-1}$. We also show for illustration $T_d = 25$ K (blue left histogram peaking at $200 M_{\odot} \text{ yr}^{-1}$). See Sect. 6.3 for details.

with $M_{500} = (10^{14} - 2 \times 10^{15}) M_{\odot}$ at $z = 0 - 0.6$ by [Lin et al. \(2012\)](#) based on *WISE* $3.4 \mu\text{m}$ photometry. M_{500} is the total mass within the central cluster regions where the mass surface density exceeds the cosmological value by at least a factor of 500. [Lin et al.](#) find that in this mass range, stellar mass scales with M_{500} as $(M_*/10^{12} M_{\odot}) = (1.8 \pm 0.1) (M_{500}/10^{14} M_{\odot})^{0.71 \pm 0.04}$. For clusters with $M_{500} = 1 \times 10^{14} M_{\odot}$ (or $2 \times 10^{15} M_{\odot}$, their highest mass), this corresponds to $M_* = 2 \times 10^{12} M_{\odot}$ (or $1.5 \times 10^{13} M_{\odot}$). We do not expect that including the intracluster light would increase these estimates by more than a few tens of percent (e.g., [Gonzalez et al. 2007](#)), which is a minor part of the uncertainty in our rough order-of-magnitude estimate.

These mass and timescale estimates suggest total star formation rates in the progenitors of massive galaxy clusters at lower redshifts of a few $\times 10^3$ and up to about $2 \times 10^4 M_{\odot} \text{ yr}^{-1}$. Using the conversion of [Kennicutt \(1998\)](#) between star formation rate and infrared luminosity (Sect. 6.3), this corresponds to $L_{\text{IR}} \simeq (10^{13} - 10^{14}) L_{\odot}$. This is well within the range of the global star formation rates and L_{FIR} values in our sample of overdensities.

For point (2), the absence of such objects, we use the [Tinker et al. \(2008\)](#) halo model to compute the expected surface density of dark matter halos. We expect between 8500 and 1×10^7 dark matter halos at $z > 2$ having masses $M_{\text{tot}} > 10^{14} M_{\odot}$ and $10^{13} M_{\odot}$, respectively, over 35% of the sky. With the assumption that the cluster galaxies have formed most of their stellar populations within a short timescale (see above), we estimate that only a fraction of those halos will be observationally caught during their intense star formation phase, when they are infrared- and submm-bright. Assuming that this phase happened mainly between $z = 5$ and $z = 1.5 - 2.0$, we find that the upper limit on the formation period of each individual cluster, about 1 Gyr, is 3–4 times shorter than the cosmic time elapsed over this epoch, 2–3 Gyr. We would therefore expect to find a few thousand dark matter halos on the submm sky at any given observing epoch. This order-of-magnitude estimate is above with our finding of about 200 overdensities with *Planck* in this study, and with a few hundred to be detected in the full *Planck* data set by [Planck](#)

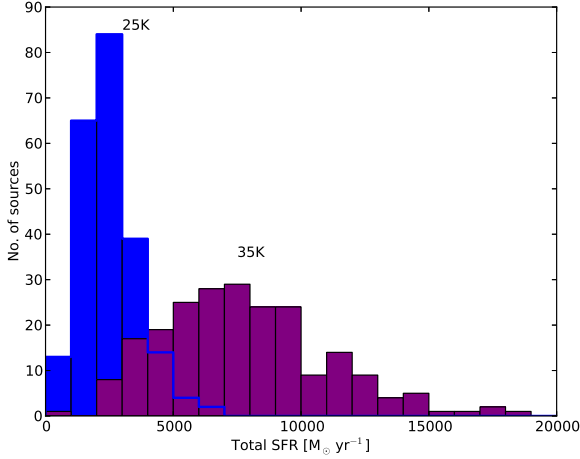


Figure 16. Total star formation rate (SFR) per *Planck* IN region, i.e., for the overdensity sample, assuming each overdensity is an actual high- z cluster of dusty galaxies, located at a redshift given by the SPIRE photometric redshift, and using a modified blackbody fit with a fixed dust temperature of $T_d = 35$ K (purple, right histogram peaking at $7 \times 10^3 M_\odot \text{ yr}^{-1}$), this temperature being favoured by the literature. We also show the total SFR for $T_d = 25$ K, giving a peak at $2 \times 10^3 M_\odot \text{ yr}^{-1}$. The structures could be intensely star-forming clusters. See Sects. 6.3 and 6.4 for details.

Collaboration (2015), but not more than an order of magnitude, illustrating the need to understand the detailed processes of star formation in the most massive halos (Bethermin et al. 2013).

7. Conclusions

Our *Planck* sample based on a colour selection of cold sources of the CIB is overwhelmingly dominated in number by significant galaxy overdensities peaking at $350 \mu\text{m}$, and a minority of rare, bright $z > 1.5$ strongly gravitationally lensed sources, among which are the brightest ever detected in the submillimetre. This confirms the efficiency of *Planck* to select extreme and rare submillimetre sources over the whole sky, as well as the need for higher angular resolution imaging using *Herschel* (and current/planned ground-based submm/mm observatories) to identify and study them.

From the analysis of *Herschel* observations of the sample of 228 *Planck* cold sources of the CIB, we draw several conclusions.

- Less than 2% of the fields are Galactic cirrus structures. When a clean and controlled selection is performed on *Planck*, there is thus no reason to expect a large cirrus contamination when using a conservative Galactic mask.
- With about 93% of the overdensities peaking at $350 \mu\text{m}$, and 3.5% peaking at $500 \mu\text{m}$, our sample unambiguously selects sky areas with the largest concentrations of red SPIRE galaxies, consisting of highly significant overdensities.
- Some of the overdensities are confirmed high- z structures, e.g., a source at $z \approx 1.7\text{--}2.0$ (Flores-Cacho et al. 2014, in prep.).
- The significance in density contrast of the overdensities (e.g., half of the fields above $10 \sigma_\delta$ when selecting red SPIRE

sources) is higher than any other sample targeting proto-clusters or high- z clusters in the submillimetre, confirming the relevance of the strategy of using *Planck* data on the cleanest parts of the sky to uncover high- z candidates.

- The SPIRE sources in the overdensity fields have a peak redshift of $z = 2$ or 1.3 , if we fix the dust temperature at $T_d = 35$ K or 25 K, respectively.
- With the assumption of $T_d = 35$ K, each SPIRE source has an average IR luminosity of $4 \times 10^{12} L_\odot$, leading to star formation rates for each source peaking at $700 M_\odot \text{ yr}^{-1}$. If confirmed, these exceptional structures harbouring vigorous star formation could be proto-clusters in their starburst phase.
- Assuming the SPIRE sources are located in the same large-scale overdensity, we derive a total IR luminosity of $4 \times 10^{13} L_\odot$, leading to total star formation rates of $7 \times 10^3 M_\odot \text{ yr}^{-1}$, and with around 10 detected sources per structure.
- About 3% of our sample is composed of intensely gravitationally lensed galaxies. This sample is unique, as it targets the brightest observed such sources, typically above 400 mJy at $350 \mu\text{m}$ and reaching up to the jansky level. They are all spectroscopically confirmed to lie at redshifts $z = 2.2\text{--}3.6$ (Canameras 2015; Nesvadba 2015).
- The novelty and efficiency of our new sample is that it provides about 50 times more fields for a *Planck-Herschel* co-analysis than in existing *Herschel* surveys searching for serendipitous *Planck* sources (e.g., Clements et al. 2014), for only a fraction of the *Herschel* observing time.
- Our new sample exhibits high density contrasts with a high significance: for the red sources, 30% of our sample (about 70 fields) shows significance levels higher than $4.5 \sigma_\delta$, and 15% of our sample (34 fields) are higher than $7 \sigma_\delta$.

The presence of the overdensities (and the hypothesis that these could be actual forming, bound structures) is consistent with other findings (Santos et al. 2014; Clements et al. 2014; Noble et al. 2013; Wylezalek et al. 2013b). Our *Planck* extraction and confirmation with *Herschel* provides an efficient selection over the whole sky, biased towards star-forming sources, giving a few hundred candidates (Fig. 15). This selection nicely complements the structures found at $z \sim 2$ already detected by different means, e.g., with the X-ray signature of hot IGM gas, with stellar mass overdensities, Ly α emission, or in association with radiogalaxies (Pentericci et al. 1997, 2000; Brodwin et al. 2005; Miley et al. 2006; Nesvadba et al. 2006; Venemans et al. 2007; Doherty et al. 2010; Papovich et al. 2010; Brodwin et al. 2010, 2011; Hatch et al. 2011; Gobat et al. 2011; Santos et al. 2011; Stanford et al. 2012; Santos et al. 2013, 2014; Brodwin et al. 2013; Galametz et al. 2013; Rigby et al. 2014; Wylezalek et al. 2013a; Chiang et al. 2014; Cooke et al. 2014; Cucciati et al. 2014). However, it is hard to estimate the fraction that may be comprised of random alignments of unrelated clumps (e.g., Chiang et al. 2013), since the fluctuation field due to clustering is highly non-Gaussian. Ancillary data (particularly redshifts) are needed to confirm the associations, and an ambitious follow-up programme is underway.

To further characterize the overdensities discovered by *Planck* and confirmed by *Herschel*, we also started to stack them in many ancillary data sets. The first data set is the *Planck* lensing map (Planck Collaboration XVII 2014). The goal is to detect a signature of the presence of large gravitational potential, as has been demonstrated already by correlating the CIB fluctuations with the lensing map (Planck Collaboration XVIII 2014). The second data set is to use the nine frequency maps and the diffuse

tSZ map obtained by MILCA (Hurier et al. 2013). The goal here is to detect a signature of the thermal Sunyaev-Zeldovich (tSZ) effect (Sunyaev & Zeldovich 1969, 1972) and thus the presence of hot gas. These analyses will be published in a subsequent paper.

The *Planck* data thus provide unique and powerful samples to uncover rare populations, exploitable for extragalactic studies, as was shown with our successful follow-up with *Herschel* of 228 *Planck* high-*z* candidates. There are hundreds more *Planck* high-*z* candidates (the full catalogue is being finalized and will be published in Planck Collaboration 2015) to be studied and characterized.

Acknowledgements. The development of *Planck* has been supported by: ESA; CNES and CNRS/INSU-IN2P3-INP (France); ASI, CNR, and INAF (Italy); NASA and DoE (USA); STFC and UKSA (UK); CSIC, MICINN, JA, and RES (Spain); Tekes, AoF, and CSC (Finland); DLR and MPG (Germany); CSA (Canada); DTU Space (Denmark); SER/SSO (Switzerland); RCN (Norway); SFI (Ireland); FCT/MCTES (Portugal); and PRACE (EU). A description of the *Planck* Collaboration and a list of its members, including the technical or scientific activities in which they have been involved, can be found at <http://www.sciops.esa.int/index.php?project=planck>.

The *Herschel* spacecraft was designed, built, tested, and launched under a contract to ESA managed by the *Herschel/Planck* Project team by an industrial consortium under the overall responsibility of the prime contractor Thales Alenia Space (Cannes), and including Astrium (Friedrichshafen) responsible for the payload module and for system testing at spacecraft level, Thales Alenia Space (Turin) responsible for the service module, and Astrium (Toulouse) responsible for the telescope, with in excess of a hundred subcontractors.

This work is based in part on observations made with the *Spitzer Space Telescope*, which is operated by the Jet Propulsion Laboratory, California Institute of Technology under a contract with NASA. Support for this work was provided by NASA through an award issued by JPL/Caltech. Based in part on observations obtained with MegaPrime/MegaCam, a joint project of CFHT and CEA/DAPNIA, at the Canada-France-Hawaii Telescope (CFHT) which is operated by the National Research Council (NRC) of Canada, the Institut National des Sciences de l'Univers of the Centre National de la Recherche Scientifique of France, and the University of Hawaii. Based in part on observations obtained with WIRCam, a joint project of CFHT, Taiwan, Korea, Canada, France, and the Canada-France-Hawaii Telescope (CFHT) which is operated by the National Research Council (NRC) of Canada, the Institut National des Sciences de l'Univers of the Centre National de la Recherche Scientifique of France, and the University of Hawaii. Based in part on observations carried out with the IRAM 30-m Telescope. IRAM is supported by INSU/CNRS (France), MPG (Germany) and IGN (Spain). Based in part on observations carried out with the IRAM Plateau de Bure Interferometer. IRAM is supported by INSU/CNRS (France), MPG (Germany) and IGN (Spain). Based in part on observations made at JCMT with SCUBA-2. The James Clerk Maxwell Telescope is operated by the Joint Astronomy Centre on behalf of the Science and Technology Facilities Council of the United Kingdom, the Netherlands Organisation for Scientific Research, and the National Research Council of Canada. This research has made use of the SIMBAD database, operated at CDS, Strasbourg, France. This research has made use of the NASA/IPAC Extragalactic Database (NED) which is operated by the Jet Propulsion Laboratory, California Institute of Technology, under contract with the National Aeronautics and Space Administration. We acknowledge the support from the CNES, the PNCG (Programme National de Cosmologie et Galaxies), ANR HUGÉ (ANR-09-BLAN-0224-HUGÉ) and ANR MULTIVERSE (ANR-11-BS56-015). We also acknowledge the support from Région Ile-de-France with DIM-ACAV. We acknowledge the Integrated Data & Operation Center (IDOC) at Institut d'Astrophysique Spatiale and Observatoire des Sciences de l'Univers de l'Université Paris Sud (OSUPS). Support for IDOC is provided by CNRS and CNES. We acknowledge final support from ASI/INAF agreement I/072/09/0 and PRIN-INAF 2012 project "Looking into the dust-obscured phase of galaxy formation through cosmic zoom lenses in the Herschel Astrophysical Large Area Survey." We acknowledge financial support from the Spanish CSIC for a JAE-DOC fellowship, co-funded by the European Social Fund and from the Ministerio de Economía y Competitividad, project AYA2012-39475-C02-01. This research made use of matplotlib Hunter (2007), and of APLpy, an open-source plotting package for Python hosted at <http://aplpy.github.com>. We thank E. Egami, B. Clément, E. Daddi, H.J. McCracken and A. Boucaud and for fruitful discussions and helpful advice.

References

- Amblard, A., Cooray, A., Serra, P., et al. 2010, *A&A*, 518, L9
 Austermann, J. E., Aretxaga, I., Hughes, D. H., et al. 2009, *MNRAS*, 393, 1573
 Barger, A. J., Cowie, L. L., Sanders, D. B., et al. 1998, *Nature*, 394, 248
 Bell, E. F. 2003, *ApJ*, 586, 794
 Bethermin, M., Dole, H., Beelen, A., & Aussel, H. 2010a, *A&A*, 512, 78
 Bethermin, M., Dole, H., Cousin, M., & Bavouzet, N. 2010b, *A&A*, 516, 43
 Bethermin, M., Dole, H., Lagache, G., Le Borgne, D., & Penin, A. 2011, *A&A*, 529, 4
 Bethermin, M., Le Floch, E., Ilbert, O., et al. 2012, *A&A*, 542, 58
 Bethermin, M., Wang, L., Dore, O., et al. 2013, *A&A*, 557, 66
 Blain, A. W., Chapman, S. C., Smail, I., & Ivison, R. 2004, *ApJ*, 611, 725
 Blain, A. W. & Longair, M. S. 1993, *MNRAS*, 264, 509
 Braglia, F. G., Ade, P. A. R., Bock, J. J., et al. 2011, *MNRAS*, 412, 1187
 Brand, K., Rawlings, S., Hill, G. J., & Lacy, M. 2003, *New Astronomy Reviews*, 47, 325
 Brodwin, M., Eisenhardt, P., Gonzalez, A., et al. 2005, *Journal of the Royal Astronomical Society of Canada*, 99, 135
 Brodwin, M., Ruel, J., Ade, P. A. R., et al. 2010, *ApJ*, 721, 90
 Brodwin, M., Stanford, S. A., Gonzalez, A. H., et al. 2013, *ApJ*, 779, 138
 Brodwin, M., Stern, D., Vikhlinin, A., et al. 2011, *ApJ*, 732, 33
 Bussmann, R. S., Perez-Fournon, I., Amber, S., et al. 2013, *ApJ*, 779, 25
 Cai, Z. Y., Lapi, A., Xia, J. Q., et al. 2013, *ApJ*, 768, 21
 Canameras, R. et al., 2015, *A&A*, in press
 Capak, P. L., Riechers, D., Scoville, N. Z., et al. 2011, *Nature*, 470, 233
 Chapin, E. L., Hughes, D. H., & Aretxaga, I. 2009, *MNRAS*, 393, 653
 Chapman, S. C., Blain, A. W., Smail, I., & Ivison, R. J. 2005, *ApJ*, 622, 772
 Chiang, Y. K., Overzier, R., & Gebhardt, K. 2013, *ApJ*, 779, 127
 Chiang, Y. K., Overzier, R., & Gebhardt, K. 2014, *ApJ*, 782, L3
 Clements, D. L., Braglia, F. G., Hyde, A. K., et al. 2014, *MNRAS*, 439, 1193
 Clements, D. L., Rigby, E., Maddox, S., et al. 2010, *A&A*, 518, L8
 Cole, S., Percival, W. J., Peacock, J. A., et al. 2005, *MNRAS*, 362, 505
 Combes, F., Rex, M., Rawle, T. D., et al. 2012, *A&A*, 538, L4
 Cooke, E. A., Hatch, N. A., Muldrew, S. I., Rigby, E. E., & Kurk, J. D. 2014, *MNRAS*, 440, 3262
 Cucciati, O., Zamorani, G., Lemaux, B. C., et al. 2014, *A&A*, 570, 16
 Daddi, E., Dannerbauer, H., Stern, D., et al. 2009, *ApJ*, 694, 1517
 Devlin, M. J., Ade, P. A. R., Aretxaga, I., et al. 2009, *Nature*, 458, 737
 Diolanti, E., Bendinelli, O., Bonaccini, D., et al. 2000, *A&AS*, 147, 335
 Doherty, M., Tanaka, M., de Breuck, C., et al. 2010, *A&A*, 509, 83
 Dole, H., Lagache, G., & Puget, J. L. 2003, *ApJ*, 585, 617
 Dole, H., Lagache, G., Puget, J. L., et al. 2006, *A&A*, 451, 417
 Eales, S. A., Raymond, G., Roseboom, I. G., et al. 2010, *A&A*, 518, L23
 Egami, E., Rex, M., Rawle, T. D., et al. 2010, *A&A*, 518, L12
 Elbaz, D., Dickinson, M., Hwang, H. S., et al. 2011, *A&A*, 533, 119
 Farrah, D., Lonsdale, C. J., Borys, C., et al. 2006, *ApJ*, 641, L17
 Ferdosi, B. J., Buddelmeijer, H., Trager, S. C., Wilkinson, M. H. F., & Roerdink, J. B. T. M. 2011, *A&A*, 531, 114
 Franceschini, A., Toffolatti, L., Mazzei, P., Danese, L., & Zotti, G. D. 1991, *A&AS*, 89, 285
 Fu, H., Jullo, E., Cooray, A., et al. 2012, *ApJ*, 753, 134
 Galametz, A., Stern, D., Pentericci, L., et al. 2013, *A&A*, 559, 2
 Galametz, M., Madden, S. C., Galliano, F., et al. 2010, *A&A*, 518, L55
 Glenn, J., Conley, A., Bethermin, M., et al. 2010, *MNRAS*, 409, 109
 Gobat, R., Daddi, E., Onodera, M., et al. 2011, *A&A*, 526, 133
 González-Nuevo, J., Argüeso, F., López-Cañiegos, M., et al. 2006, *MNRAS*, 369, 1603
 Gonzalez, A. H., Zaritsky, D., & Zabludoff, A. I. 2007, *ApJ*, 666, 147
 Greve, T. R., Vieira, J. D., Weiß, A., et al. 2012, *ApJ*, 756, 101
 Griffin, M. J., Abergel, A., Abreu, A., et al. 2010, *A&A*, 518, L3
 Guiderdoni, B., Bouchet, F. R., Puget, J. L., Lagache, G., & Hivon, E. 1997, *Nature*, 390, 257
 Harris, A. I., Baker, A. J., Frayer, D. T., et al. 2012, *ApJ*, 752, 152
 Harrison, I. & Coles, P. 2012, *MNRAS*, 421, L19
 Hatch, N. A., de Breuck, C., Galametz, A., et al. 2011, *MNRAS*, 410, 1537
 Hauser, M. G., Arendt, R. G., Kelsall, T., et al. 1998, *ApJ*, 508, 25
 Hauser, M. G. & Dwek, E. 2001, *ARA&A*, 37, 249
 Herranz, D., González-Nuevo, J., Clements, D. L., et al. 2013, *A&A*, 549, 31
 Hezaveh, Y. D., Marrone, D. P., & Holder, G. P. 2012, *ApJ*, 761, 20
 Holz, D. E. & Perlmutter, S. 2012, *ApJ*, 755, L36
 Hughes, D. H., Serjeant, S., Dunlop, J., et al. 1998, *Nature*, 394, 241
 Hunter, J. D. 2007, *Computing In Science & Engineering*, 9, 90
 Hurier, G., Macias-Perez, J. F., & Hildebrandt, S. 2013, *A&A*, 558, 118
 Hutsi, G. 2010, *MNRAS*, 401, 2477
 Ivison, R. J., Smail, I., Amblard, A., et al. 2012, *MNRAS*, 425, 1320
 Ivison, R. J., Swinbank, A. M., Smail, I., et al. 2013, *ApJ*, 772, 137
 Kashlinsky, A. 2005, *Phys. Rep.*, 409, 361

Kennicutt, R. C. 1998, *ARA&A*, 36, 189
 Kodama, T., Tanaka, I., Kajisawa, M., et al. 2007, *MNRAS*, 377, 1717
 Kuiper, E., Hatch, N. A., Venemans, B. P., et al. 2011, *MNRAS*, 1376, 1376
 Lagache, G., Puget, J. L., & Dole, H. 2005, *ARA&A*, 43, 727
 Lima, M., Jain, B., & Devlin, M. 2010, *MNRAS*, 406, 2352
 Lin, Y. T., Stanford, S. A., Eisenhardt, P. R. M., et al. 2012, *ApJ*, 745, L3
 Magdis, G. E., Daddi, E., Bethermin, M., et al. 2012, *ApJ*, 760, 6
 Magdis, G. E., Elbaz, D., Hwang, H. S., et al. 2010, *MNRAS*, 409, 22
 Magliocchetti, M., Silva, L., Lapi, A., et al. 2007, *MNRAS*, 375, 1121
 Magnelli, B., Lutz, D., Saintonge, A., et al. 2014, *A&A*, 561, 86
 Mei, S., Scarlata, C., Pentericci, L., et al. 2014, Star-forming blue ETGs in two newly discovered galaxy overdensities in the HUDF at $z=1.84$ and 1.9 : unveiling the progenitors of passive ETGs in cluster cores, arXiv:1403.7524
 Miley, G. & de Breuck, C. 2008, *Astronomy and Astrophysics Review*, 15, 67
 Miley, G. K., Overzier, R. A., Zirm, A. W., et al. 2006, *ApJ*, 650, L29
 Miville-Deschênes, M. A. & Lagache, G. 2005, *Astrophys. J. Suppl. Ser.*, 157, 302
 Montier, L. A. & Giard, M. 2005, *A&A*, 439, 35
 Montier, L. A., Pelkonen, V. M., Juvela, M., Ristorcelli, I., & Marshall, D. J. 2010, *A&A*, 522, 83
 Muzzin, A., Wilson, G., Demarco, R., et al. 2013, *ApJ*, 767, 39
 Negrello, M., Gonzalez-Nuevo, J., Magliocchetti, M., et al. 2005, *MNRAS*, 358, 869
 Negrello, M., Hopwood, R., de Zotti, G., et al. 2010, *Science*, 330, 800
 Negrello, M., Perrotta, F., González-Nuevo, J., et al. 2007, *MNRAS*, 377, 1557
 Nesvadba, N. et al., 2015, *A&A*, in prep
 Nesvadba, N. P. H., Lehnert, M. D., Eisenhauer, F., et al. 2006, *ApJ*, 650, 693
 Neugebauer, G., Habing, H. J., van Duinen, R., et al. 1984, *ApJ*, 278, L1
 Nguyen, H. T., Schulz, B., Levenson, L., et al. 2010, *A&A*, 518, L5
 Noble, A. G., Geach, J. E., van Engelen, A. J., et al. 2013, *MNRAS*, 436, L40
 Oliver, S. J., Wang, L., Smith, A. J., et al. 2010, *A&A*, 518, L21
 Ott, S. 2010, in *Astronomical Data Analysis Software and Systems XIX.*, ed. K.-I. M. Yoshihiko Mizumoto & M. Ohishi (San Francisco: Astronomical Society of the Pacific, 2010., p.139: ASP Conference Series), 139
 Paciga, G., Scott, D., & Chapin, E. L. 2009, *MNRAS*, 395, 1153
 Papovich, C. 2008, *ApJ*, 676, 206
 Papovich, C., Momcheva, I., Willmer, C. N. A., et al. 2010, *ApJ*, 716, 1503
 Patanchon, G., Ade, P. A. R., Bock, J. J., et al. 2009, *ApJ*, 707, 1750
 Pentericci, L., Kurk, J. D., Roettgering, H. J. A., et al. 2000, *A&A*, 361, L25
 Pentericci, L., Roettgering, H. J. A., Miley, G. K., Carilli, C. L., & McCarthy, P. 1997, *A&A*, 326, 580
 Pilbratt, G. L., Riedinger, J. R., Passvogel, T., et al. 2010, *A&A*, 518, L1
 Pisani, A. 1996, *MNRAS*, 278, 697
 Planck Collaboration, . 2015, in prep
 Planck Collaboration. 2011, *The Explanatory Supplement to the Planck Early Release Compact Source Catalogue (ESA)*
 Planck Collaboration I. 2011, *A&A*, 536, A1
 Planck Collaboration VII. 2011, *A&A*, 536, A7
 Planck Collaboration XVIII. 2011, *A&A*, 536, A18
 Planck Collaboration I. 2014, *A&A*, 571, A1
 Planck Collaboration VI. 2014, *A&A*, 571, A6
 Planck Collaboration VII. 2014, *A&A*, 571, A7
 Planck Collaboration XVI. 2014, *A&A*, 571, A16
 Planck Collaboration XVII. 2014, *A&A*, 571, A17
 Planck Collaboration XVIII. 2014, *A&A*, 571, A18
 Planck Collaboration XX. 2014, *A&A*, 571, A20
 Planck Collaboration XXVIII. 2014, *A&A*, 571, A28
 Planck Collaboration XXX. 2014, *A&A*, 571, A30
 Planck Collaboration I. 2015, *A&A*, submitted
 Planck Collaboration XIII. 2015, *A&A*, submitted
 Planck Collaboration Int. VII. 2013, *A&A*, 550, A133
 Pope, A. & Chary, R. R. 2010, *ApJ*, 715, L171
 Puget, J. L., Abergel, A., Bernard, J. P., et al. 1996, *A&A*, 308, L5
 Rawle, T. D., Egami, E., Bussmann, R. S., et al. 2014, *ApJ*, 783, 59
 Renzini, A. 2006, *ARA&A*, 44, 141
 Rettura, A., Martinez-Manso, J., Stern, D., et al. 2014, *ApJ*, 797, 109
 Rigby, E. E., Hatch, N. A., Röttgering, H. J. A., et al. 2014, *MNRAS*, 437, 1882
 Rudnick, G., von Der Linden, A., Pellä, R., et al. 2009, *ApJ*, 700, 1559
 Santos, J. S., Altieri, B., Popesso, P., et al. 2013, *MNRAS*, 433, 1287
 Santos, J. S., Altieri, B., Tanaka, M., et al. 2014, *MNRAS*, 438, 2565
 Santos, J. S., Fassbender, R., Nastasi, A., et al. 2011, *A&A*, 531, L15
 Scoville, N., Aussel, H., Benson, A., et al. 2007, *Astrophys. J. Suppl. Ser.*, 172, 150
 Stanford, S. A., Brodwin, M., Gonzalez, A. H., et al. 2012, *ApJ*, 753, 164
 Stanford, S. A., Gonzalez, A. H., Brodwin, M., et al. 2014, *Astrophys. J. Suppl. Ser.*, 213, 25
 Steidel, C. C., Adelberger, K. L., Shapley, A. E., et al. 2000, *ApJ*, 532, 170
 Sunyaev, R. A. & Zeldovich, Y. B. 1969, *Nature*, 223, 721

Sunyaev, R. A. & Zeldovich, Y. B. 1972, *Comments on Astrophysics and Space Physics*, 4, 173
 Symeonidis, M., Vaccari, M., Berta, S., et al. 2013, *MNRAS*, 431, 2317
 Tegmark, M., Strauss, M. A., Blanton, M. R., et al. 2004, *Phys. Rev. D*, 69, 3501
 Tinker, J., Kravtsov, A. V., Klypin, A., et al. 2008, *ApJ*, 688, 709
 Trindade, A. M. M., Avelino, P. P., & Viana, P. T. P. 2013, *MNRAS*, 435, 782
 Valtchanov, I., Altieri, B., Berta, S., et al. 2013, *MNRAS*, 436, 2505
 Venemans, B. P., Roettgering, H. J. A., Miley, G. K., et al. 2007, *A&A*, 461, 823
 Vieira, J. D., Crawford, T. M., Switzer, E. R., et al. 2010, *ApJ*, 719, 763
 Viero, M. P., Moncelsi, L., Quadri, R. F., et al. 2013, *ApJ*, 779, 32
 Waizmann, J. C., Redlich, M., & Bartelmann, M. 2012, *A&A*, 547, 67
 Wardlow, J. L., Cooray, A., de Bernardis, F., et al. 2013, *ApJ*, 762, 59
 Weiss, A., de Breuck, C., Marrone, D. P., et al. 2013, *ApJ*, 767, 88
 Williamson, R., Benson, B. A., High, F. W., et al. 2011, *ApJ*, 738, 139
 Wright, E. L., Eisenhardt, P. R. M., Mainzer, A. K., et al. 2010, *AJ*, 140, 1868
 Wylezalek, D., Galametz, A., Stern, D., et al. 2013a, *ApJ*, 769, 79
 Wylezalek, D., Vernet, J., de Breuck, C., et al. 2013b, *MNRAS*, 428, 3206

Appendix A: SPIRE band-merging procedure

Table A.1. Percentages of SPIRE sources matched at 250 and 500 μm from the 350 μm input SPIRE catalogue, and the frequency of matches (i.e., number of sources found per 350 μm source). Here, IN refers to the *Planck* source region, and OUT refers to the zone outside the *Planck* 50% contour (see Sect. 2.3). The rows are: no match (top); one match; two matches; and three matches (bottom). More than 60% of the SPIRE 350 μm sources corresponding to the *Planck* sources (i.e., the IN regions) have counterparts at 250 and 500 μm .

	250 μm		500 μm	
	IN	OUT	IN	OUT
No match	10.9	16.7	38.8	67.0
1 match	82.0	77.0	60.7	32.9
2 matches	6.9	6.0	0.5	0.1
3 matches	0.1	0.2	0	0

Table A.2. After the SPIRE band-merging process, the percentage of SPIRE sources that do not have any flux density measurement (i.e., are blended or not detected or have multiple matches in Table A.1). More than about 90% of the *Planck* IN sources have counterparts at all three SPIRE wavelengths.

	250 μm		350 μm		500 μm	
	IN	OUT	IN	OUT	IN	OUT
No detections	0.2 %	0.6 %	0.2 %	0.6 %	0.5 %	3.6 %
S/N < 3	3.2 %	7.6 %	0.9 %	3.2 %	10.6 %	39.4 %

We describe here the details of the band-merging procedure, highlighted in Sect. 3.3.

First step: positional optimization of blind catalogues using shorter wavelength data.

- Apply a 4σ cut to the 350 μm blind catalogue obtained with *StarFinder* (Sect. 3.2). This cut is imposed to obtain a high purity of detections.
- Match by position the 350 μm sources to the 250 μm catalogue, within a radius of one 250 μm FWHM.

The following depends on whether there are 0, 1, 2, or more matches:

- if zero sources are found at $250\ \mu\text{m}$, this is a non-detection at $250\ \mu\text{m}$;
- if one source is found, we take this source to be the $250\ \mu\text{m}$ counterpart;
- if two sources are found, we replace the position of the $350\ \mu\text{m}$ unique source by the two positions of the $250\ \mu\text{m}$ sources (the $350\ \mu\text{m}$ flux density will be measured later) and take the two $250\ \mu\text{m}$ flux densities;
- we apply the same procedure for triply or more matched sources: we keep the positions of the $250\ \mu\text{m}$ sources as priors (only one case, outside the *Planck* beam).

We repeat this operation at $500\ \mu\text{m}$ using one $350\ \mu\text{m}$ FWHM as the search radius. The statistics of those basic positional matches are reported in Table A.1. We have more than 60% unique matches in the IN regions, i.e., for the *Planck* sources. This simple method is, however, biasing the sample towards strong and unique detections at the three SPIRE wavelengths. The two following steps address this issue.

Second step: prior flux density determination.

- At $350\ \mu\text{m}$: take the StarFinder flux densities (Sect. 3.2) for single-matched source with $250\ \mu\text{m}$; assign $S_{350} = 0$ if there are two or more matched sources at $250\ \mu\text{m}$.
- At $250\ \mu\text{m}$: take the flux density for single-, double- or triple-matched sources with the $350\ \mu\text{m}$ source; assign $S_{250} = 0$ if there is no match with $350\ \mu\text{m}$ at this step.
- At $500\ \mu\text{m}$: take the StarFinder flux densities (Sect. 3.2) for single-matched source with the $350\ \mu\text{m}$ source; Assign $S_{500} = 0$ if there are 0, 2 or more matched sources at $350\ \mu\text{m}$.

Third step: deblending and photometry using FastPhot.

- Use the $250\ \mu\text{m}$ positions obtained in the first step as prior positions.
- Use flux densities at each SPIRE wavelength obtained in the second step.
- Perform simultaneous PSF-fitting and deblending;
- Assign the measured flux densities that were previously missing.

Table A.2 presents some statistics following the band-merging process.

Appendix B: SPIRE number counts tables

The measured number counts shown in Fig. 5, are provided in tables B.1, B.2, and B.3. We note that those counts are not corrected for incompleteness or for flux boosting, since here we are interested only in the relative distribution of the samples (and the quantification of the excess of one sample to another).

Appendix C: Number counts by type: overdensity or lensed sources

As discussed in Sect. 4.4, Fig. C.1 represents the counts for overdensity fields (left) and lensed fields (right). This shows that the bright part of the number counts is dominated by single bright objects, i.e., the lensed sources. However, these lensed counts cannot be used for statistical studies of the lensed sources because we have only used the surface area of the *Planck* IN region.

Appendix D: Overdensities using AKDE

We can also use another estimator for the density contrast δ_{350} by taking the measured source density from AKDE. If we compute the density minus the median density divided by the median density, we obtain the distribution shown in Fig. D.1.

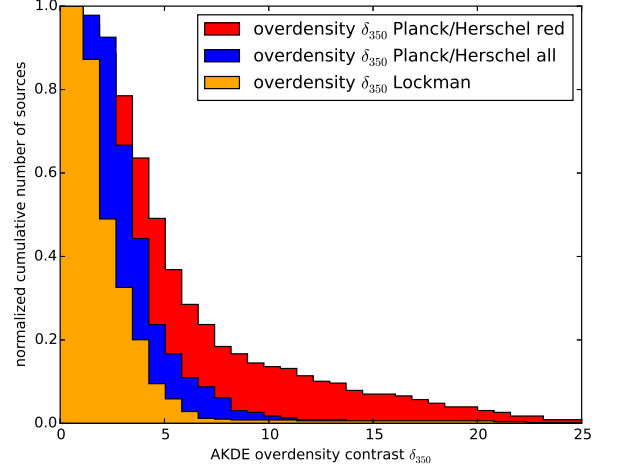


Figure D.1. Cumulative histogram of the normalized overdensity contrast δ_{350} using the AKDE density estimator. Blue represents all our SPIRE sources, red represents only redder SPIRE sources, defined by $S_{350}/S_{250} > 0.7$ and $S_{500}/S_{350} > 0.6$, and orange 500 random fields in Lockman. Most of our fields show overdensities larger than 5. See Sect. 4.2 for details.

Appendix E: Gallery of selected sources

We provide 3-colour images for a few sources drawn from the 228 of our sample. Each plot shows:

- a 3-colour image of the SPIRE data, with $250\ \mu\text{m}$ in blue, $350\ \mu\text{m}$ in green, and $500\ \mu\text{m}$ in red (using the python APLpy module: `show_rgb`);
- the *Planck* contour (IN region, i.e., 50% of the peak) as a bold white line;
- the significance of the SPIRE overdensity contrast (starting at 2σ , and then incrementing by 1σ) as yellow solid lines.

Figure E summarizes the 228 SPIRE sample.

- ¹ APC, AstroParticule et Cosmologie, Université Paris Diderot, CNRS/IN2P3, CEA/Irfu, Observatoire de Paris, Sorbonne Paris Cité, 10, rue Alice Domon et Léonie Duquet, 75205 Paris Cedex 13, France
- ² African Institute for Mathematical Sciences, 6-8 Melrose Road, Muizenberg, Cape Town, South Africa
- ³ Agenzia Spaziale Italiana Science Data Center, Via del Politecnico snc, 00133, Roma, Italy
- ⁴ Agenzia Spaziale Italiana, Viale Liegi 26, Roma, Italy
- ⁵ Aix Marseille Université, CNRS, LAM (Laboratoire d'Astrophysique de Marseille) UMR 7326, 13388, Marseille, France
- ⁶ Astrophysics Group, Cavendish Laboratory, University of Cambridge, J J Thomson Avenue, Cambridge CB3 0HE, U.K.

Table B.1. Differential Euclidean-normalized number counts $S^{2.5} \frac{dN}{dS}$ at $250 \mu\text{m}$, not corrected for incompleteness or flux boosting. They are given here only for relative distributions.

$\langle S_{250} \rangle$ [mJy]	S_{250} range [mJy]	IN [Jy ^{1.5} sr ⁻¹]	Planck [Jy ^{1.5} sr ⁻¹]	OUT [Jy ^{1.5} sr ⁻¹]	Planck [Jy ^{1.5} sr ⁻¹]	Total [Jy ^{1.5} sr ⁻¹]	Planck [Jy ^{1.5} sr ⁻¹]	Lockman [Jy ^{1.5} sr ⁻¹]	HLS [Jy ^{1.5} sr ⁻¹]
11.	11.- 12.	–	–	–	–	–	–	–	–
12.	12.- 13.	–	–	–	–	–	–	–	20. ± 7.
13.	13.- 14.	–	–	–	–	–	–	–	103. ± 14.
16.	14.- 17.	–	–	–	–	–	–	–	271. ± 21.
19.	17.- 21.	235. ± 50.	476. ± 28.	445. ± 25.	–	–	–	–	447. ± 27.
25.	21.- 29.	9276. ± 343.	6075. ± 108.	6493. ± 104.	4828. ± 122.	750. ± 38.	–	–	–
34.	29.- 40.	40486. ± 838.	21789. ± 238.	24227. ± 234.	29237. ± 351.	3299. ± 94.	–	–	–
50.	40.- 59.	37392. ± 1001.	18877. ± 275.	21291. ± 273.	23910. ± 395.	15891. ± 257.	–	–	–
75.	59.- 90.	19583. ± 944.	10611. ± 269.	11781. ± 264.	13593. ± 388.	11697. ± 288.	–	–	–
116.	90.- 141.	7545. ± 791.	4960. ± 248.	5297. ± 239.	6494. ± 362.	6011. ± 278.	–	–	–
182.	141.- 223.	3482. ± 742.	2587. ± 248.	2704. ± 236.	3696. ± 377.	3127. ± 277.	–	–	–
290.	223.- 357.	935. ± 540.	1963. ± 303.	1829. ± 273.	2730. ± 455.	1891. ± 303.	–	–	–
467.	357.- 576.	626. ± 626.	1785. ± 409.	1634. ± 365.	1524. ± 482.	975. ± 308.	–	–	–
753.	576.- 931.	5100. ± 2550.	573. ± 331.	1164. ± 440.	310. ± 310.	1190. ± 486.	–	–	–

Table B.2. Differential Euclidean-normalized number counts $S^{2.5} \frac{dN}{dS}$ at $350 \mu\text{m}$, not corrected for incompleteness or flux boosting. They are given here only for relative distributions.

$\langle S_{350} \rangle$ [mJy]	S_{350} range [mJy]	IN [Jy ^{1.5} sr ⁻¹]	Planck [Jy ^{1.5} sr ⁻¹]	OUT [Jy ^{1.5} sr ⁻¹]	Planck [Jy ^{1.5} sr ⁻¹]	Total [Jy ^{1.5} sr ⁻¹]	Planck [Jy ^{1.5} sr ⁻¹]	Lockman [Jy ^{1.5} sr ⁻¹]	HLS [Jy ^{1.5} sr ⁻¹]
11.	11.- 12.	–	–	–	–	–	–	–	–
12.	12.- 13.	–	–	–	–	–	–	–	–
13.	13.- 14.	–	–	–	–	–	–	–	5. ± 3.
16.	14.- 17.	–	–	–	–	–	–	–	39. ± 8.
19.	17.- 21.	107. ± 34.	162. ± 16.	155. ± 15.	–	–	–	–	148. ± 16.
25.	21.- 29.	7931. ± 317.	4114. ± 88.	4611. ± 87.	648. ± 45.	415. ± 29.	–	–	–
34.	29.- 40.	32868. ± 755.	13424. ± 187.	15959. ± 190.	19667. ± 288.	3661. ± 99.	–	–	–
50.	40.- 59.	31093. ± 913.	10831. ± 209.	13473. ± 217.	16222. ± 325.	8986. ± 194.	–	–	–
75.	59.- 90.	16805. ± 875.	4650. ± 178.	6235. ± 192.	6880. ± 276.	4938. ± 187.	–	–	–
116.	90.- 141.	3731. ± 556.	1305. ± 127.	1622. ± 132.	1936. ± 198.	1509. ± 140.	–	–	–
182.	141.- 223.	1425. ± 475.	783. ± 136.	867. ± 134.	809. ± 176.	640. ± 126.	–	–	–
290.	223.- 357.	1247. ± 623.	561. ± 162.	650. ± 163.	303. ± 152.	339. ± 128.	–	–	–
467.	357.- 576.	1879. ± 1085.	94. ± 94.	327. ± 163.	305. ± 216.	195. ± 138.	–	–	–
753.	576.- 931.	6374. ± 2851.	382. ± 270.	1164. ± 440.	–	–	–	–	–

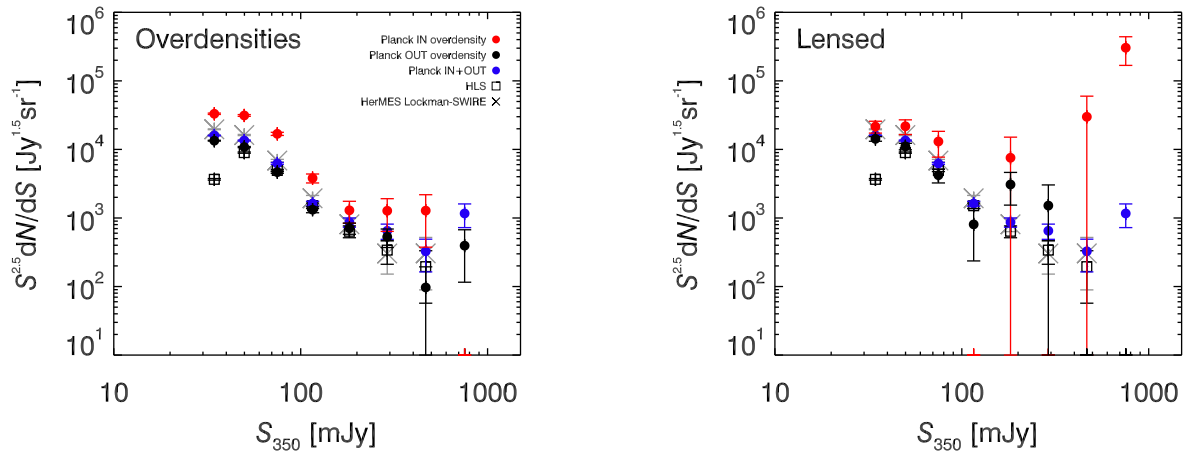

Figure C.1. Differential Euclidean-normalized number counts, $S^{2.5} \frac{dN}{dS}$, for various data sets at $350 \mu\text{m}$, to illustrate the difference between the overdensity fields (left) and the lensed fields (right). This is the same as Fig. 5, except that we have split the fields into only overdensity fields and only lensed fields. Lensed sources thus dominate the statistics at large flux densities, while overdensities dominate at smaller flux densities. See Sect 4.4 for details.

Table B.3. Differential Euclidean-normalized number counts $S^{2.5} \frac{dN}{dS}$ at $500 \mu\text{m}$, not corrected for incompleteness or flux boosting. They are given here only for relative distributions.

$\langle S_{500} \rangle$ [mJy]	S_{500} range [mJy]	IN [Jy ^{1.5} sr ⁻¹]	<i>Planck</i> [Jy ^{1.5} sr ⁻¹]	OUT [Jy ^{1.5} sr ⁻¹]	<i>Planck</i> [Jy ^{1.5} sr ⁻¹]	Total [Jy ^{1.5} sr ⁻¹]	<i>Planck</i> [Jy ^{1.5} sr ⁻¹]	Lockman [Jy ^{1.5} sr ⁻¹]	HLS [Jy ^{1.5} sr ⁻¹]
11.	11.- 12.	–	–	–	–	–	–	–	–
12.	12.- 13.	–	–	–	–	–	–	–	–
13.	13.- 14.	–	–	–	–	–	–	–	–
16.	14.- 17.	–	–	–	–	–	–	–	3. ± 2.
19.	17.- 21.	–	–	5. ± 3.	4. ± 2.	–	–	–	42. ± 8.
25.	21.- 29.	685. ± 93.	346. ± 26.	390. ± 25.	–	–	–	–	138. ± 17.
34.	29.- 40.	13397. ± 482.	3474. ± 95.	4768. ± 104.	4614. ± 140.	437. ± 34.	–	–	1964. ± 90.
50.	40.- 59.	15600. ± 647.	2890. ± 108.	4547. ± 126.	5692. ± 193.	935. ± 81.	–	–	1964. ± 90.
75.	59.- 90.	5875. ± 517.	751. ± 72.	1419. ± 92.	1473. ± 128.	935. ± 81.	–	–	935. ± 81.
116.	90.- 141.	1078. ± 299.	199. ± 50.	314. ± 58.	484. ± 99.	232. ± 55.	–	–	232. ± 55.
182.	141.- 223.	791. ± 354.	142. ± 58.	227. ± 68.	77. ± 54.	172. ± 65.	–	–	172. ± 65.
290.	223.- 357.	1559. ± 697.	140. ± 81.	325. ± 115.	76. ± 76.	97. ± 69.	–	–	97. ± 69.
467.	357.- 576.	2506. ± 1253.	94. ± 94.	408. ± 183.	–	–	–	–	–
753.	576.- 931.	3825. ± 2208.	–	499. ± 288.	–	–	–	–	–

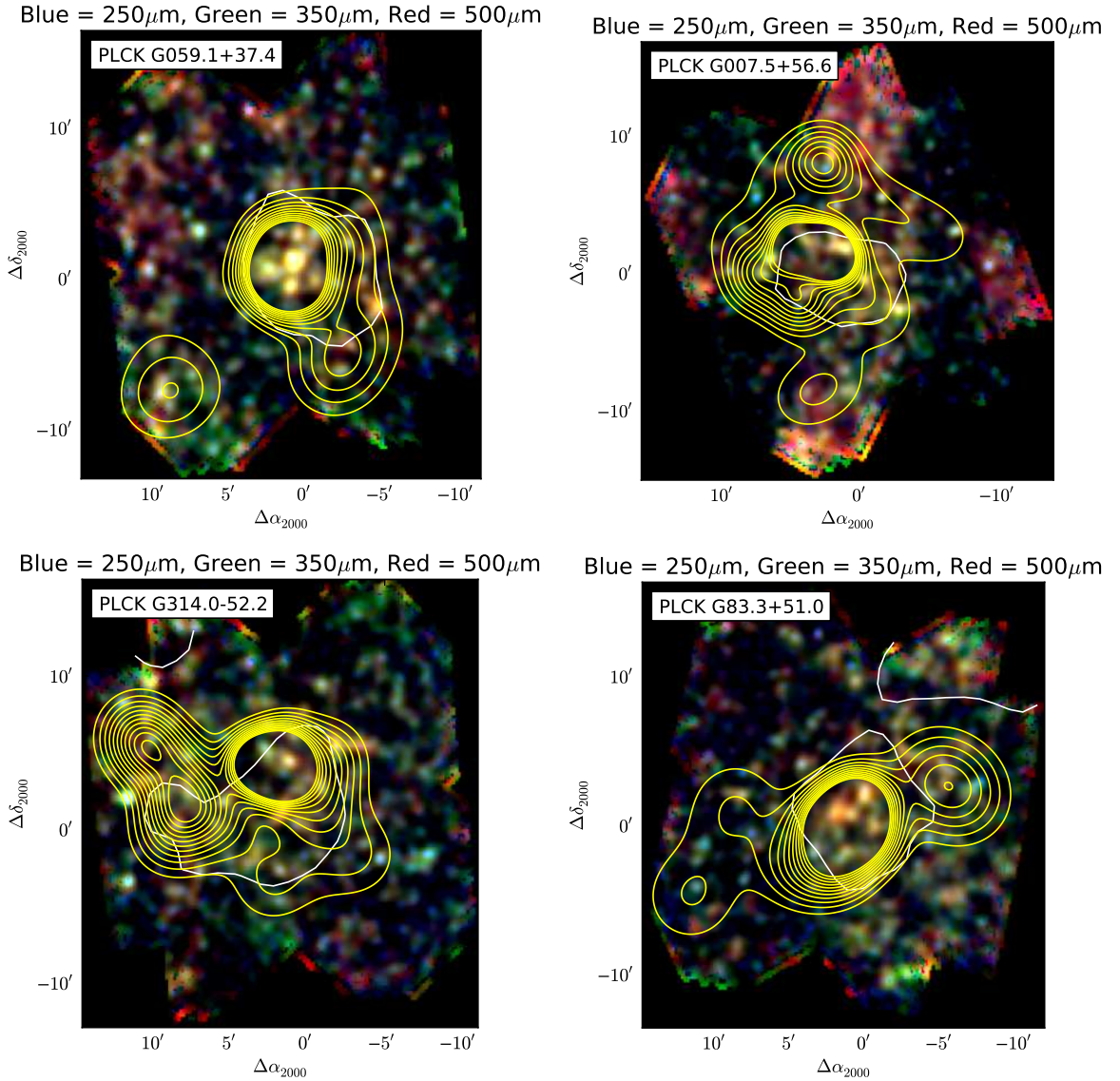


Figure E.1. Representative *Planck* targets, showing 3-colour SPIRE images: blue, $250 \mu\text{m}$; green, $350 \mu\text{m}$; and red, $500 \mu\text{m}$. The white contours show the *Planck* IN region, while the yellow contours are the significance of the overdensity of $350 \mu\text{m}$ sources, plotted 2σ , 3σ , 4σ , etc.

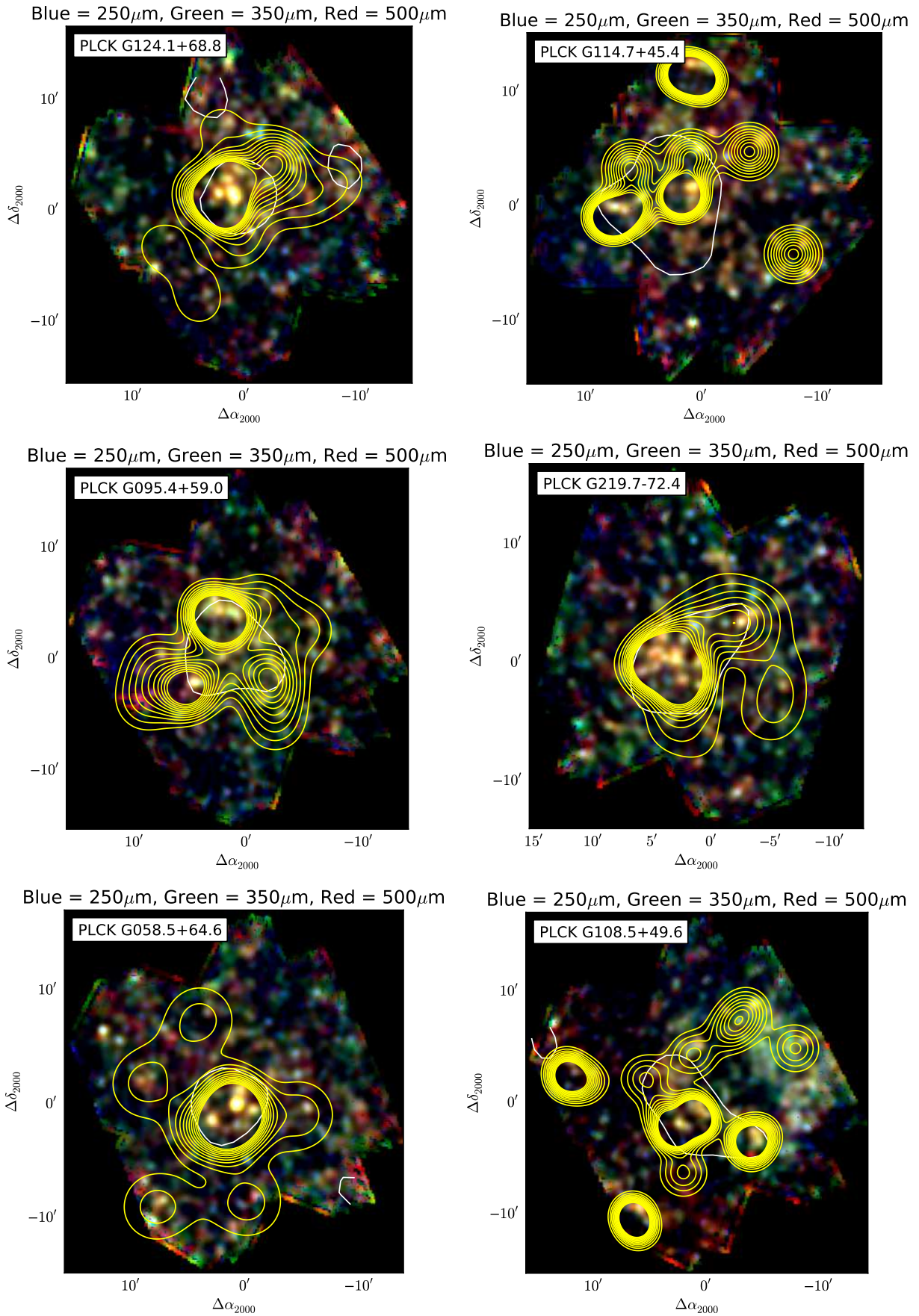


Figure E.2. Representative *Planck* targets. Same as Fig. E.1.

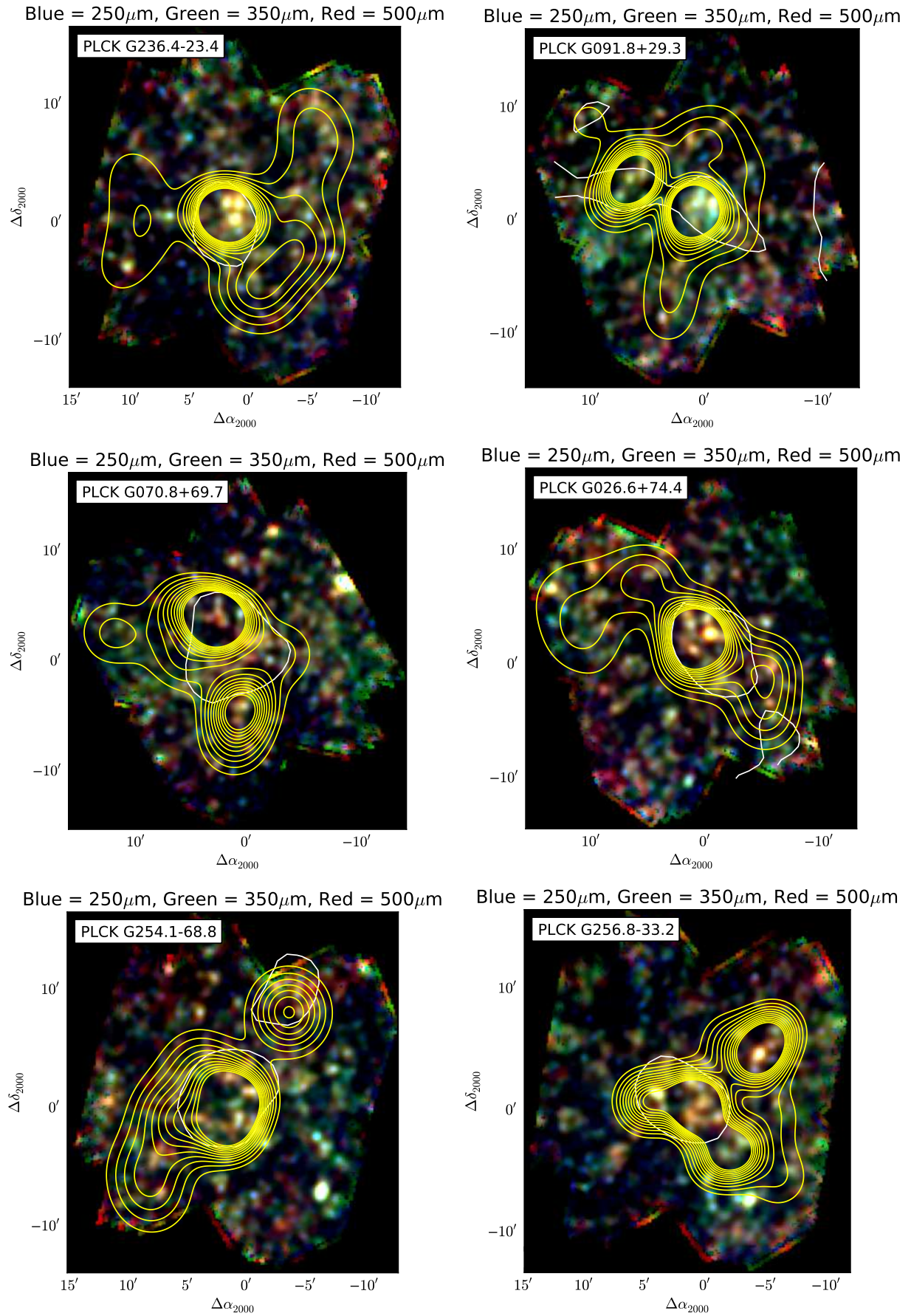


Figure E.3. Representative *Planck* targets. Same as Fig. E.1.

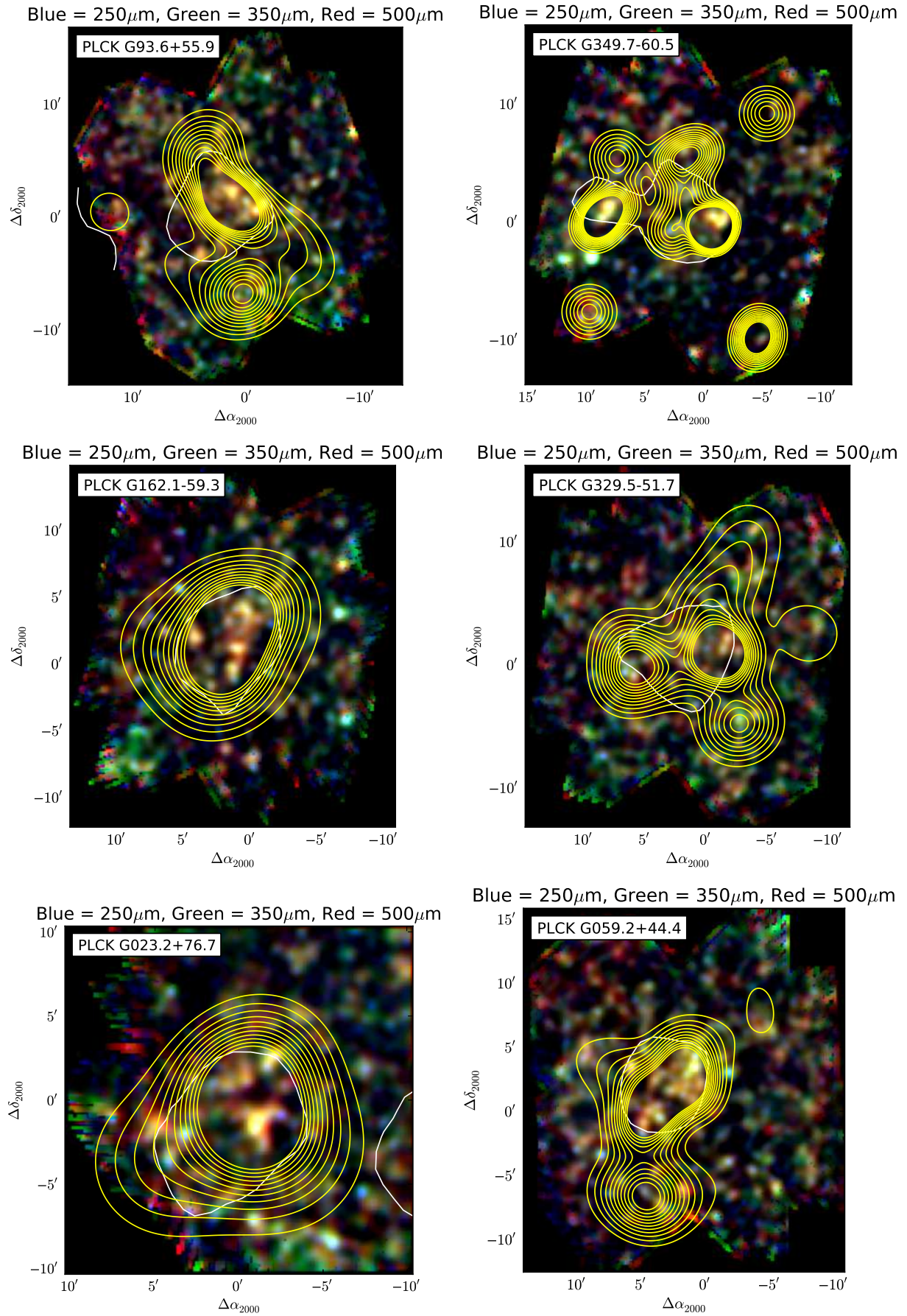


Figure E.4. Representative *Planck* targets. Same caption as Fig. E.1.

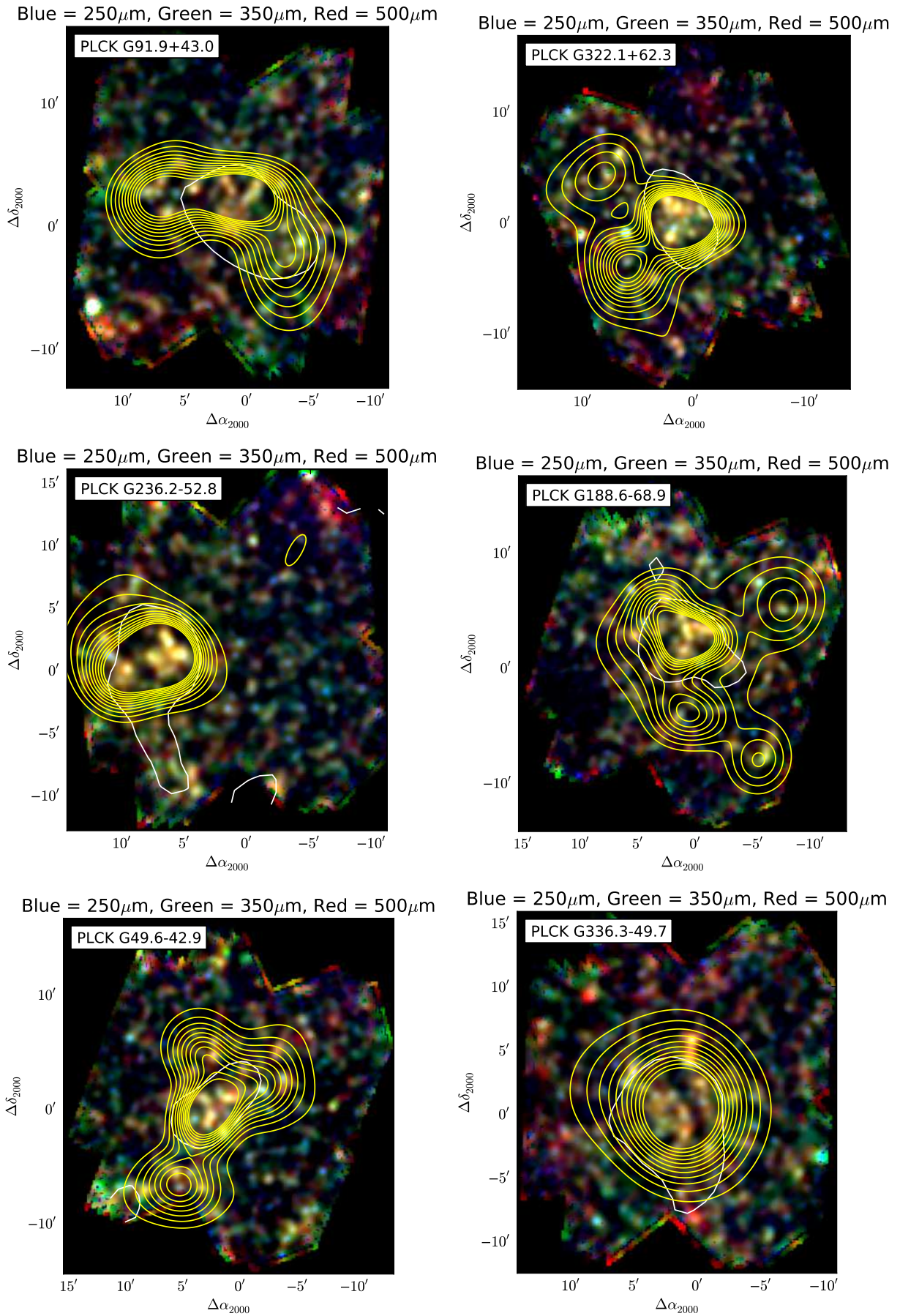


Figure E.5. Representative *Planck* targets. Same caption as Fig. E.1.

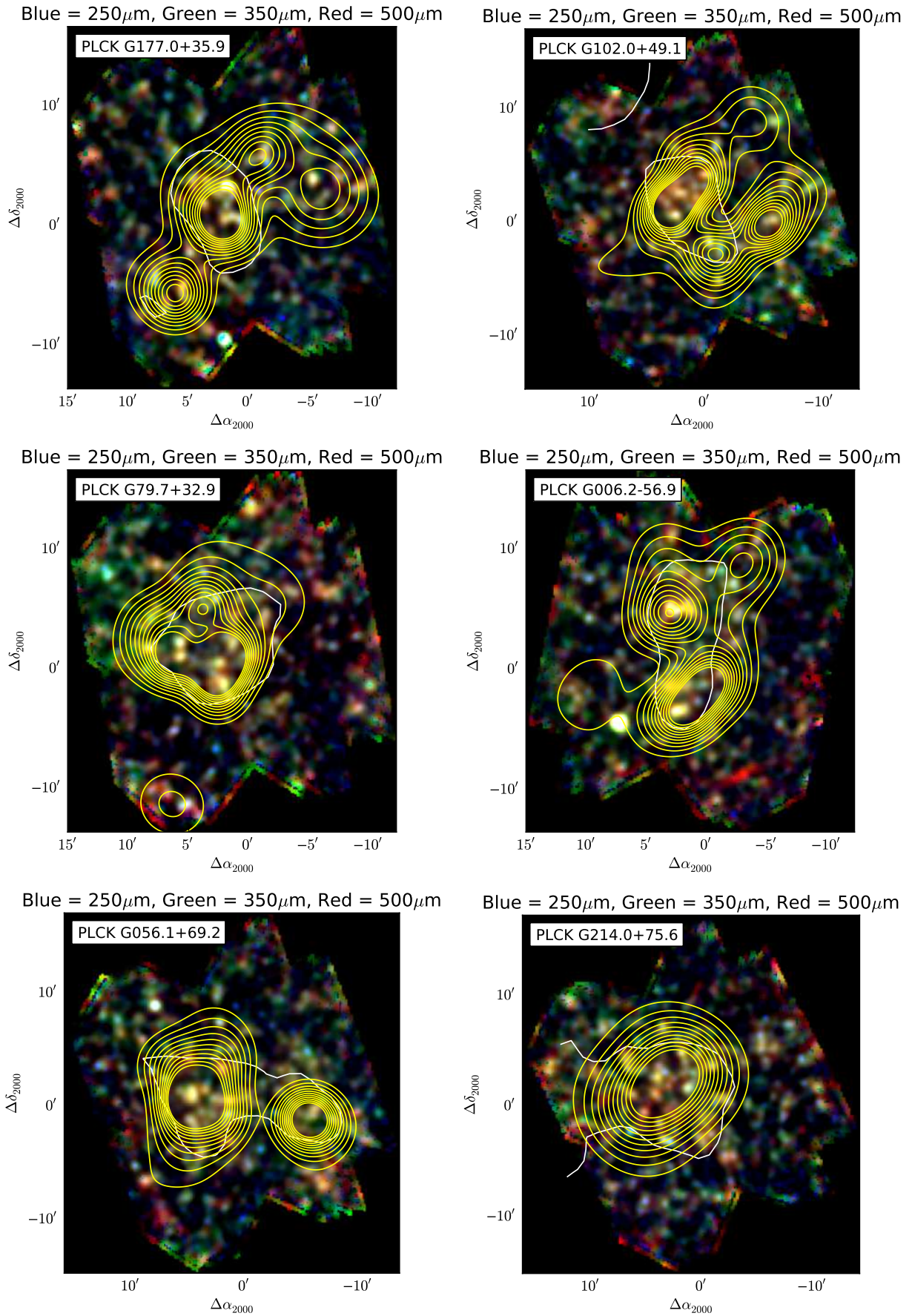


Figure E.6. Representative *Planck* targets. Same caption as Fig. E.1.

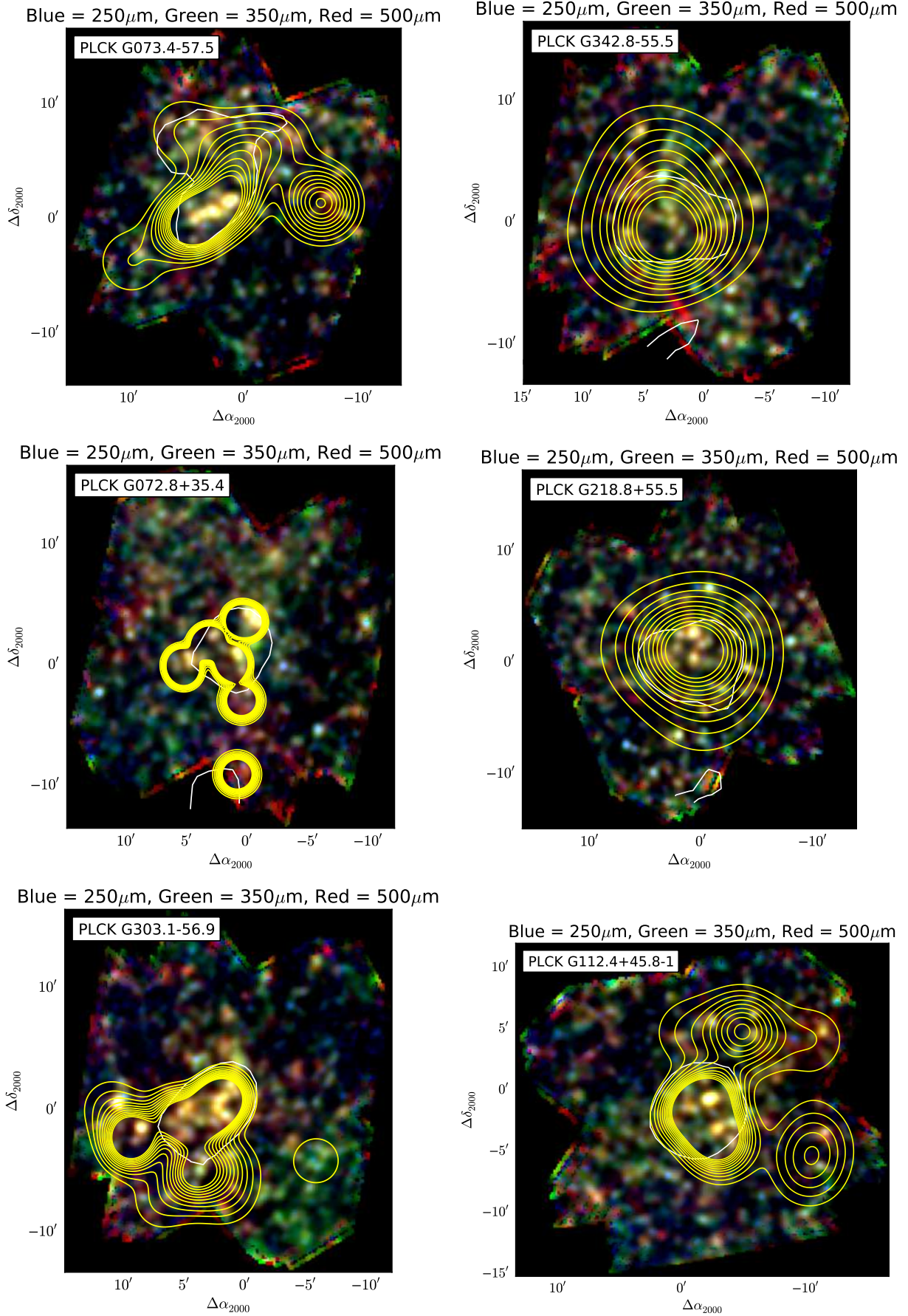


Figure E.7. Representative *Planck* targets. Same caption as Fig. E.1.

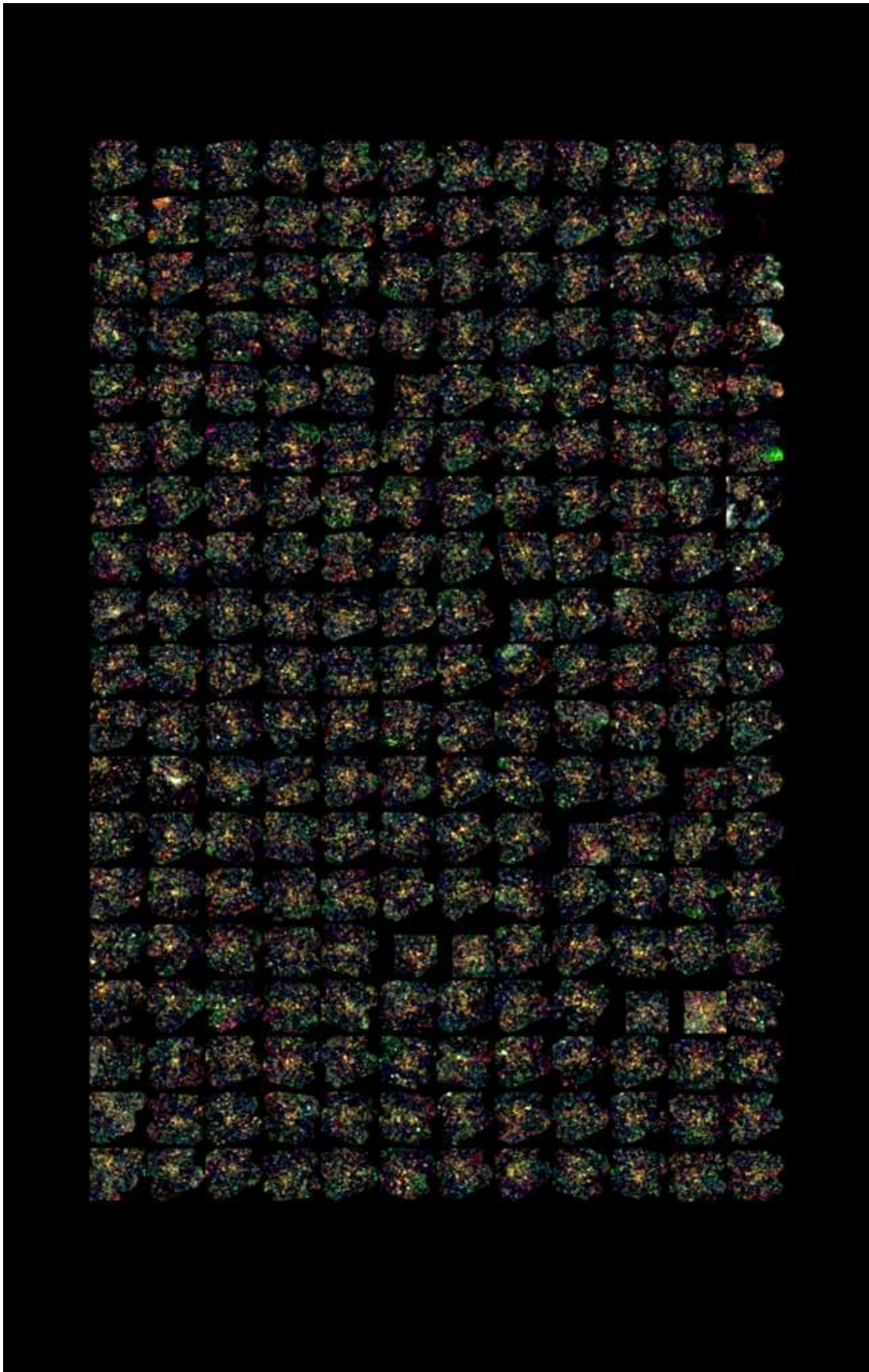


Figure E.8. Mosaic showing the 228 SPIRE fields.

- ⁷ Astrophysics & Cosmology Research Unit, School of Mathematics, Statistics & Computer Science, University of KwaZulu-Natal, Westville Campus, Private Bag X54001, Durban 4000, South Africa
- ⁸ Atacama Large Millimeter/submillimeter Array, ALMA Santiago Central Offices, Alonso de Cordova 3107, Vitacura, Casilla 763 0355, Santiago, Chile
- ⁹ CITA, University of Toronto, 60 St. George St., Toronto, ON M5S 3H8, Canada
- ¹⁰ CNRS, IRAP, 9 Av. colonel Roche, BP 44346, F-31028 Toulouse cedex 4, France
- ¹¹ California Institute of Technology, Pasadena, California, U.S.A.
- ¹² Centro de Estudios de Física del Cosmos de Aragón (CEFCA), Plaza San Juan, 1, planta 2, E-44001, Teruel, Spain
- ¹³ Computational Cosmology Center, Lawrence Berkeley National Laboratory, Berkeley, California, U.S.A.
- ¹⁴ DSM/Irfu/SPP, CEA-Saclay, F-91191 Gif-sur-Yvette Cedex, France
- ¹⁵ DTU Space, National Space Institute, Technical University of Denmark, Elektrovej 327, DK-2800 Kgs. Lyngby, Denmark
- ¹⁶ Département de Physique Théorique, Université de Genève, 24, Quai E. Ansermet, 1211 Genève 4, Switzerland
- ¹⁷ Departamento de Física, Universidad de Oviedo, Avda. Calvo Sotelo s/n, Oviedo, Spain
- ¹⁸ Department of Astronomy and Department of Physics, University of Illinois at Urbana-Champaign, 1002 West Green Street, Urbana, Illinois, U.S.A.
- ¹⁹ Department of Astrophysics/IMAPP, Radboud University Nijmegen, P.O. Box 9010, 6500 GL Nijmegen, The Netherlands
- ²⁰ Department of Physics & Astronomy, University of British Columbia, 6224 Agricultural Road, Vancouver, British Columbia, Canada
- ²¹ Department of Physics and Astronomy, University College London, London WC1E 6BT, U.K.
- ²² Department of Physics, Florida State University, Keen Physics Building, 77 Chieftan Way, Tallahassee, Florida, U.S.A.
- ²³ Department of Physics, Gustaf Hällströmin katu 2a, University of Helsinki, Helsinki, Finland
- ²⁴ Department of Physics, Princeton University, Princeton, New Jersey, U.S.A.
- ²⁵ Department of Physics, University of California, Santa Barbara, California, U.S.A.
- ²⁶ Department of Physics, University of Illinois at Urbana-Champaign, 1110 West Green Street, Urbana, Illinois, U.S.A.
- ²⁷ Dipartimento di Fisica e Astronomia G. Galilei, Università degli Studi di Padova, via Marzolo 8, 35131 Padova, Italy
- ²⁸ Dipartimento di Fisica e Scienze della Terra, Università di Ferrara, Via Saragat 1, 44122 Ferrara, Italy
- ²⁹ Dipartimento di Fisica, Università La Sapienza, P. le A. Moro 2, Roma, Italy
- ³⁰ Dipartimento di Fisica, Università degli Studi di Milano, Via Celoria, 16, Milano, Italy
- ³¹ Dipartimento di Fisica, Università degli Studi di Trieste, via A. Valerio 2, Trieste, Italy
- ³² Dipartimento di Fisica, Università di Roma Tor Vergata, Via della Ricerca Scientifica, 1, Roma, Italy
- ³³ Discovery Center, Niels Bohr Institute, Blegdamsvej 17, Copenhagen, Denmark
- ³⁴ European Southern Observatory, ESO Vitacura, Alonso de Cordova 3107, Vitacura, Casilla 19001, Santiago, Chile
- ³⁵ European Space Agency, ESAC, Camino bajo del Castillo, s/n, Urbanización Villafranca del Castillo, Villanueva de la Cañada, Madrid, Spain
- ³⁶ European Space Agency, ESAC, Planck Science Office, Camino bajo del Castillo, s/n, Urbanización Villafranca del Castillo, Villanueva de la Cañada, Madrid, Spain
- ³⁷ European Space Agency, ESTEC, Keplerlaan 1, 2201 AZ Noordwijk, The Netherlands
- ³⁸ Facoltà di Ingegneria, Università degli Studi e-Campus, Via Isimbardi 10, Novedrate (CO), 22060, Italy
- ³⁹ Gran Sasso Science Institute, INFN, viale F. Crispi 7, 67100 L'Aquila, Italy
- ⁴⁰ HGSFP and University of Heidelberg, Theoretical Physics Department, Philosophenweg 16, 69120, Heidelberg, Germany
- ⁴¹ Helsinki Institute of Physics, Gustaf Hällströmin katu 2, University of Helsinki, Helsinki, Finland
- ⁴² INAF - Osservatorio Astrofisico di Catania, Via S. Sofia 78, Catania, Italy
- ⁴³ INAF - Osservatorio Astronomico di Padova, Vicolo dell'Osservatorio 5, Padova, Italy
- ⁴⁴ INAF - Osservatorio Astronomico di Roma, via di Frascati 33, Monte Porzio Catone, Italy
- ⁴⁵ INAF - Osservatorio Astronomico di Trieste, Via G.B. Tiepolo 11, Trieste, Italy
- ⁴⁶ INAF/IASF Bologna, Via Gobetti 101, Bologna, Italy
- ⁴⁷ INAF/IASF Milano, Via E. Bassini 15, Milano, Italy
- ⁴⁸ INFN, Sezione di Bologna, Via Irnerio 46, I-40126, Bologna, Italy
- ⁴⁹ INFN, Sezione di Roma 1, Università di Roma Sapienza, Piazzale Aldo Moro 2, 00185, Roma, Italy
- ⁵⁰ INFN/National Institute for Nuclear Physics, Via Valerio 2, I-34127 Trieste, Italy
- ⁵¹ Imperial College London, Astrophysics group, Blackett Laboratory, Prince Consort Road, London, SW7 2AZ, U.K.
- ⁵² Infrared Processing and Analysis Center, California Institute of Technology, Pasadena, CA 91125, U.S.A.
- ⁵³ Institut Universitaire de France, 103, bd Saint-Michel, 75005, Paris, France
- ⁵⁴ Institut d'Astrophysique Spatiale, CNRS (UMR8617) Université Paris-Sud 11, Bâtiment 121, Orsay, France
- ⁵⁵ Institut d'Astrophysique de Paris, CNRS (UMR7095), 98 bis Boulevard Arago, F-75014, Paris, France
- ⁵⁶ Institute for Space Sciences, Bucharest-Magurale, Romania
- ⁵⁷ Institute of Astronomy, University of Cambridge, Madingley Road, Cambridge CB3 0HA, U.K.
- ⁵⁸ Institute of Theoretical Astrophysics, University of Oslo, Blindern, Oslo, Norway
- ⁵⁹ Instituto de Física de Cantabria (CSIC-Universidad de Cantabria), Avda. de los Castros s/n, Santander, Spain
- ⁶⁰ Istituto Nazionale di Fisica Nucleare, Sezione di Padova, via Marzolo 8, I-35131 Padova, Italy
- ⁶¹ Jet Propulsion Laboratory, California Institute of Technology, 4800 Oak Grove Drive, Pasadena, California, U.S.A.
- ⁶² Jodrell Bank Centre for Astrophysics, Alan Turing Building, School of Physics and Astronomy, The University of Manchester, Oxford Road, Manchester, M13 9PL, U.K.
- ⁶³ Kavli Institute for Cosmology Cambridge, Madingley Road, Cambridge, CB3 0HA, U.K.
- ⁶⁴ LAL, Université Paris-Sud, CNRS/IN2P3, Orsay, France
- ⁶⁵ LERMA, CNRS, Observatoire de Paris, 61 Avenue de l'Observatoire, Paris, France
- ⁶⁶ Laboratoire AIM, IRFU/Service d'Astrophysique - CEA/DSM - CNRS - Université Paris Diderot, Bât. 709, CEA-Saclay, F-91191 Gif-sur-Yvette Cedex, France
- ⁶⁷ Laboratoire Traitement et Communication de l'Information, CNRS (UMR 5141) and Télécom ParisTech, 46 rue Barrault F-75634 Paris Cedex 13, France
- ⁶⁸ Laboratoire de Physique Subatomique et Cosmologie, Université Grenoble-Alpes, CNRS/IN2P3, 53, rue des Martyrs, 38026 Grenoble Cedex, France
- ⁶⁹ Laboratoire de Physique Théorique, Université Paris-Sud 11 & CNRS, Bâtiment 210, 91405 Orsay, France
- ⁷⁰ Lawrence Berkeley National Laboratory, Berkeley, California, U.S.A.
- ⁷¹ Lebedev Physical Institute of the Russian Academy of Sciences, Astro Space Centre, 84/32 Profsoyuznaya st., Moscow, GSP-7, 117997, Russia
- ⁷² Max-Planck-Institut für Astrophysik, Karl-Schwarzschild-Str. 1, 85741 Garching, Germany

- ⁷³ McGill Physics, Ernest Rutherford Physics Building, McGill University, 3600 rue University, Montréal, QC, H3A 2T8, Canada
- ⁷⁴ National University of Ireland, Department of Experimental Physics, Maynooth, Co. Kildare, Ireland
- ⁷⁵ Niels Bohr Institute, Blegdamsvej 17, Copenhagen, Denmark
- ⁷⁶ Observational Cosmology, Mail Stop 367-17, California Institute of Technology, Pasadena, CA, 91125, U.S.A.
- ⁷⁷ Optical Science Laboratory, University College London, Gower Street, London, U.K.
- ⁷⁸ Paris, France
- ⁷⁹ SISSA, Astrophysics Sector, via Bonomea 265, 34136, Trieste, Italy
- ⁸⁰ School of Physics and Astronomy, Cardiff University, Queens Buildings, The Parade, Cardiff, CF24 3AA, U.K.
- ⁸¹ Sorbonne Université-UPMC, UMR7095, Institut d'Astrophysique de Paris, 98 bis Boulevard Arago, F-75014, Paris, France
- ⁸² Space Research Institute (IKI), Russian Academy of Sciences, Profsoyuznaya Str, 84/32, Moscow, 117997, Russia
- ⁸³ Space Sciences Laboratory, University of California, Berkeley, California, U.S.A.
- ⁸⁴ Special Astrophysical Observatory, Russian Academy of Sciences, Nizhnij Arkhyz, Zelenchukskiy region, Karachai-Cherkessian Republic, 369167, Russia
- ⁸⁵ Steward Observatory, University of Arizona, Tucson, AZ, U.S.A.
- ⁸⁶ Sub-Department of Astrophysics, University of Oxford, Keble Road, Oxford OX1 3RH, U.K.
- ⁸⁷ UPMC Univ Paris 06, UMR7095, 98 bis Boulevard Arago, F-75014, Paris, France
- ⁸⁸ Université de Toulouse, UPS-OMP, IRAP, F-31028 Toulouse cedex 4, France
- ⁸⁹ Universities Space Research Association, Stratospheric Observatory for Infrared Astronomy, MS 232-11, Moffett Field, CA 94035, U.S.A.
- ⁹⁰ University of Granada, Departamento de Física Teórica y del Cosmos, Facultad de Ciencias, Granada, Spain
- ⁹¹ University of Granada, Instituto Carlos I de Física Teórica y Computacional, Granada, Spain
- ⁹² Warsaw University Observatory, Aleje Ujazdowskie 4, 00-478 Warszawa, Poland